



1  **High metabolic zinc demand within native Amundsen and Ross Sea phytoplankton**
2 **communities determined by stable isotope uptake rate measurements**

3 Riss M. Kell^{1,+}, Rebecca J. Chmiel¹, Deepa Rao¹, Dawn M. Moran¹, Matthew R. McIlvin¹,
4 Tristan J. Horner¹, Nicole L. Schanke³, Robert B. Dunbar², Giacomo R. DiTullio³, Mak A. Saito¹

5 ¹Department of Marine Chemistry and Geochemistry, Woods Hole Oceanographic Institution,
6 Woods Hole, MA, USA

7 ²Doerr School of Sustainability, Stanford University, Stanford, CA 94305

8 ³Hollings Marine Laboratory, College of Charleston, Charleston, South Carolina, 29412, USA

9 *Correspondence to:* Mak A. Saito (msaito@whoi.edu)

10 ⁺Formerly published under Riss Kellogg; now affiliated with Gloucester Marine Genomics
11 Institute, Gloucester MA, 01930-3006

12 **Abstract**

13 Zinc (Zn) is an essential micronutrient for most eukaryotic phytoplankton. Zn uptake by
14 phytoplankton within the euphotic zone results in nutrient-like dissolved Zn profiles (dZn) with a
15 large dynamic range. The combination of key biochemical uses for Zn and large vertical
16 gradients in dZn implies the potential for rapid rates of Zn removal from the surface ocean.
17 However, due to the ease of contamination at sea, direct measurements of dZn uptake within
18 natural environments have not been previously made. To investigate the demand for dZn and for
19 dissolved cadmium (dCd; a closely related nutrient-like element) within Southern Ocean
20 phytoplankton communities, we conducted ⁶⁷Zn and ¹¹⁰Cd tracer uptake experiments within the
21 Amundsen Sea, Ross Sea, and Terra Nova Bay into the >3 µm phytoplankton particulate size
22 fraction. The highly productive Amundsen Sea and Ross Sea of Antarctica host large
23 phytoplankton blooms in the austral spring and summer, during which macronutrient and



24 micronutrient surface concentrations become significantly depleted largely due to phytoplankton
25 uptake. In autumn and winter, nutrient levels are “reset” to high concentrations throughout the
26 water column in these environments due to convective overturn, advancing sea ice cover, and
27 darkness. This annual “resetting” of nutrient concentrations makes these Antarctic environments
28 ideal locations to study the seasonal demand for Zn within these productive communities.

29 In this study, variations in metal uptake rates over depth and time and correlations with
30 other oceanic parameters were examined. High total metal uptake rates (ρ_{Metal}) of both Zn and
31 Cd were consistent with the observed depletion of dZn and dCd surface concentrations. Our
32 findings suggest that high biomass and low seawater pCO_2 exerted primary control over
33 increasing ρ_{Zn} , which in turn led to increases in ρ_{Cd} likely through the upregulation of shared
34 transport systems. Overall, we observed a high magnitude of Zn uptake ($> 100 \text{ pmol dZn L}^{-1} \text{ d}^{-1}$)
35 into the particulate phase within these Southern Ocean phytoplankton communities, suggesting
36 that even in the Zn-rich waters of the Southern Ocean, high Zn uptake rates can lead to Zn
37 depletion and potential Zn scarcity.

38 **1 Introduction**

39 Zinc (Zn) is an essential trace metal micronutrient for marine phytoplankton with roles in
40 carbon fixation, organic phosphorus uptake, and transcriptional and translational processes,
41 among others (Shaked et al. 2006; Morel et al. 2013, 2020; Twining and Baines 2013). Nutrient-
42 like depth profiles of total dissolved Zn (dZn) are characterized by depleted surface
43 concentrations due to uptake by phytoplankton within the euphotic zone, reflecting this high
44 biological demand (Fitzwater et al. 2000; Lohan et al. 2002; Zhao et al. 2014; Middag et al.
45 2019). Zn is particularly important as a catalytic cofactor in carbonic anhydrase (CA)
46 metalloenzymes, which catalyze the reversible dehydration of HCO_3^- to CO_2 . As HCO_3^-



47 constitutes about 90% of the dissolved inorganic carbon (DIC) pool in the surface ocean, CAs in
48 marine algae are a critical part of the carbon concentrating mechanism (CCM) that maintains a
49 CO_2 supply to the carbon-fixing enzyme ribulose-1,5-biphosphate carboxylase/oxygenase
50 (RUBISCO). Less abundant divalent metal cations such as cobalt (Co^{2+}) and cadmium (Cd^{2+})
51 can replace Zn^{2+} in some algal CA subtypes (Lane et al. 2005), conferring biochemical flexibility
52 to algae confronted with low Zn bioavailability.

53 While Cd is known to cause toxic effects in most organisms (Brand et al. 1986; Das et al.
54 1997), dCd depth profiles are also nutrient-like. As noted above, the biological use of Cd as a
55 catalytic cofactor within Cd-containing carbonic anhydrase (ζ -CA, or CDCA) likely contributes
56 to surface dCd depletion and thus to the observed nutrient-like profiles, though this remains the
57 only known biological use of Cd to date (Lee and Morel 1995; Sunda and Huntsman 2000; Haas
58 et al. 2009). It has also been proposed that phytoplankton may assimilate Cd abiotically—this
59 mode of Cd uptake is non-specific, a case of ‘mistaken identity’ in which phytoplankton bind
60 and store imported Cd inside the cell to avoid toxicity, coupling the cycling of Cd to the
61 biological cycle of nutrients (Horner et al. 2013). As the beneficial effect of adding Cd to
62 phytoplankton cultures has only been observed when Zn is limiting (Price and Morel 1990; Lee
63 et al. 1995; Xu et al. 2007), it has been speculated that the ability to use Cd in place of Zn in
64 CDCA may confer a competitive advantage to Zn-limited algae under low pCO_2 . To date,
65 homolog *cdca* genes have been found exclusively in diatom species (Park et al. 2007, 2008).
66 However, since the beneficial effect of Cd has also been observed in organisms such as the green
67 alga *Tetraselmis maculata* and the coccolithophore *Emiliania huxleyi* that lack the *cdca* gene
68 (Lee and Morel 1995), it is thought that Cd may have other biochemical functions in
69 phytoplankton still awaiting discovery.



70 Globally, dZn concentrations share a near-linear correlation with those of dissolved
71 silicate (Bruland et al. 1978), a macronutrient required by diatoms to form their siliceous
72 frustules. While this would seem to suggest that Zn is predominantly present in and
73 remineralized simultaneously with siliceous diatom frustules at depth, this is not the case. Only a
74 small fraction of cellular Zn (1-3%) is incorporated into frustules (Ellwood and Hunter 2000)
75 while the majority of Zn is instead associated with diatom organic matter (Twining et al. 2004).
76 Furthermore, cellular Zn within sinking diatom detritus is remineralized over the same short
77 length-scale as phosphorus (P) as opposed to the greater depths at which siliceous material
78 remineralizes (Twining et al. 2014).

79 Hypotheses to explain the coupling of Zn and Si generally propose that a combination of
80 physical and biogeochemical processes (including reversible adsorption of Zn onto sinking
81 organic particles (Weber et al. 2018)) give rise to the Zn:Si relationship, with strong Zn
82 drawdown by Southern Ocean diatoms and the resulting export of Zn-rich biogenic particles
83 acting as a key influence (Vance et al. 2017). This is complemented by the observation that
84 Southern Ocean diatom species possess cellular Zn quotas that are 3-15x higher compared to
85 those of low-latitude species (Twining and Baines 2013), and Zn is rapidly stripped from
86 Southern Ocean surface waters (Ellwood 2008; Zhao et al. 2014). This rapid removal of Zn may
87 be, in part, due to low seawater pCO₂ resulting from bloom conditions during austral summer
88 that further exacerbates the need for inorganic carbon acquisition by photosynthetic
89 phytoplankton, which in turn exacerbates Zn demand through its use as a cofactor in carbonic
90 anhydrase (Kell et al. 2023). Ocean biogeochemical modeling studies have demonstrated that
91 model variants with high (> 4.5 mmol:mol) Zn:P uptake ratios are able to reproduce the Zn-Si
92 correlation without any explicit coupling between Zn and Si (Vance et al. 2017; de Souza et al.



93 2018; Roshan et al. 2018), suggesting that rapid Zn removal into the particulate phase is a key
94 feature of biogeochemical cycling in the Southern Ocean.

95 The rapid removal of dZn from the surface within the Southern Ocean suggests the
96 possibility for phytoplankton growth to become Zn-limited. While phytoplankton growth in the
97 Southern Ocean is well-known to be primarily limited by Fe availability (Martin 1990; Arrigo et
98 al. 2008), melting icebergs and ice shelves are known to act as external sources of Fe (St-Laurent
99 et al. 2017; Hopwood et al. 2019; Person et al. 2021) with larger Fe inputs expected from
100 increased ice melt in a warming climate. Increased dFe inputs to surface Antarctic waters may
101 act to relieve Fe stress, but would simultaneously support the development of other nutrient
102 limitations. For example, low availabilities of both dZn and vitamin B₁₂ have been previously
103 observed to co-limit phytoplankton growth with Fe in the Ross Sea (Bertrand et al. 2007; Kell et
104 al. 2023). A high demand for Zn naturally exists within eukaryotic phytoplankton due to the
105 requirement for Zn²⁺ in numerous metabolic functions— therefore, without similarly enhanced
106 inputs of dZn to the water column, the alleviation of primary Fe limitation could induce Zn stress
107 as the next most in-demand metal micronutrient. Coastal polynyas that form within the
108 Amundsen and Ross Seas during austral spring and summer are particularly primed to
109 experience Zn stress as these regions host highly productive seasonal phytoplankton blooms that
110 act as significant carbon sinks (Arrigo et al. 2012). This high productivity draws pCO₂ down to
111 low levels (< 200 ppm), putting pressure on the carbon concentrating mechanism of
112 photosynthetic phytoplankton to acquire CO₂ and thus to acquire Zn as the predominantly
113 utilized metal cofactor within carbonic anhydrases.

114 The present study enhances our knowledge of what constitutes the anticipated high levels
115 of Zn uptake in the Southern Ocean with empirical field data measured within native Southern



116 Ocean phytoplankton communities. This study developed a field-based, stable Zn isotope uptake
117 rate method, building on a prior stable Cd uptake rate method (Cox et al. 2014). While Zn uptake
118 has been measured in laboratory cultures (Sunda and Huntsman 1992, 1995, 2000), and the
119 influence of grazing and trophic transfer studies have been conducted using radioactive isotopes
120 (Hutchins and Bruland 1994, 1995), to our knowledge direct measurements of Zn uptake in
121 natural marine phytoplankton communities have not been conducted previously, despite interest
122 in modeling its biogeochemical uptake and cycling (Weber et al. 2018). We measured the total
123 uptake rates of Zn and Cd along the shelves of the Amundsen Sea and Ross Sea during the
124 austral summer of 2017-2018 (December – March). This was accomplished by introducing ^{67}Zn
125 and ^{110}Cd (with natural abundances of 4.10% and 12.5%, respectively) into short-term (24 hr)
126 incubation experiments. The aim was to quantify the transfer of dissolved $^{110}\text{Cd}^{2+}$ and $^{67}\text{Zn}^{2+}$ into
127 the particulate fraction exceeding 3 μm . Both stable isotopes can be used as uptake tracers by
128 analysis of isotope abundances that deviate from natural abundances within the particulate phase.
129 The transfer of added isotopes into the particulate phase is the combined result of 1) active
130 transport of metal into cells, 2) nonspecific metal adsorption to cell surfaces, 3) metal adsorption
131 to non-living particulate organic matter, and 4) metal adsorption to particulate inorganic matter,
132 though we expect active transport into cells to dominate the measured particulate isotopic signal
133 due to the high abundance of actively growing autotrophic cells in the photic zone observed in
134 the Southern Ocean during austral summer. These measurements of uptake rates were then used
135 to infer timescales of surface dZn and dCd depletion in these Antarctic environments. These
136 uptake rates contribute to understanding the biological demand and potential for Zn limitation of
137 primary productivity in highly productive coastal environments, such as the polynyas
138 surrounding Antarctica (Kell et al. 2023).

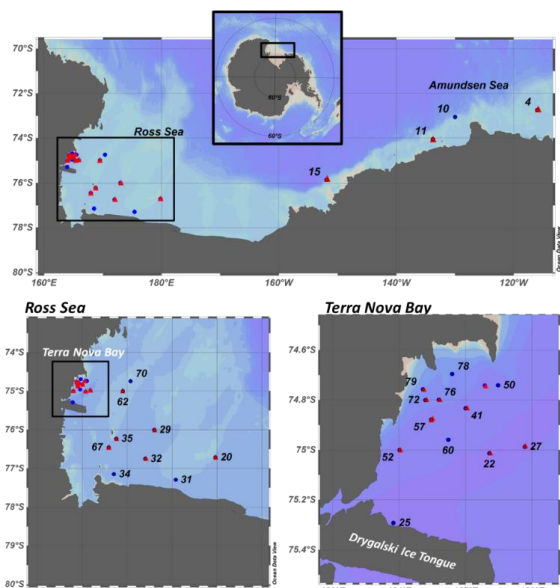


139

140 **2 Materials and methods**

141 **2.1 Study area and sample collection**

142 Samples were collected during the CICLOPS (Cobalamin and Iron Co-Limitation of
143 Phytoplankton Species) expedition (NBP18-01) aboard the RVIB *Nathaniel B. Palmer*,
144 December 11, 2017 – March 3, 2018 in the Amundsen Sea and Ross Sea of the Southern Ocean
145 (**Fig. 1**).



146

147 **Figure 1.** Map showing the stations sampled over the course of the CICLOPS cruise. Stations
148 marked by red triangles indicate those at which stable ^{67}Zn and ^{110}Cd uptake rate experiments
149 were performed. An expanded map of stations sampled in the Ross Sea is shown at bottom left,
150 while a further expansion of stations sampled in Terra Nova Bay is shown at bottom right.
151

152 Station metadata is given in **Table S1**. Water samples were collected using trace metal
153 clean (TMC) sampling protocols described previously (Cutter and Bruland 2012). A TMC
154 rosette suspended on a Kevlar line and equipped with twelve 8L X-Niskin bottles (Ocean Test
155 Equipment) was used to collect seawater at depths ranging from 10 – 600 m. Continuous



156 underway measurements of pCO₂ measurements at ~5 m depth were taken using a pCO₂
157 measurement system from Lamont-Doherty Earth Observatory (LDEO, 0.017/sec rate).
158 Hydrography data were collected using sensors deployed on a titanium trace metal rosette
159 (TMR) in tandem with TMC niskin bottles. The TMR was equipped with sensors to measure
160 temperature, conductivity, pressure, dissolved oxygen, chlorophyll (Chl) fluorescence, altimetry,
161 beam transmission, and photosynthetically active irradiance (PAR). Chl fluorescence was
162 measured using a WetLabs ECO-FL fluorometer. A complete data report and sensor list are
163 available at [NBP1801DATA.pdf \(rvdata.us\)](#). Mixed layer depth (MLD) was determined for each
164 station within Terra Nova Bay as the first depth at which the difference between the potential
165 density (σ_0) and reference density (the potential density at 10m, σ_{ref}) was greater than or equal to
166 0.125 kg m⁻³ (Bishop and Wood 2009; Ohnemus et al. 2017).

167 **2.2 Preparation of plasticware**

168 Polyethylene and polycarbonate sampling and incubation bottles were rigorously cleaned
169 to remove trace metal contaminants before use. Bottles were rinsed with Milli-Q water
170 (Millipore), soaked for 72h in <1% Citranox detergent, rotated, soaked for an additional 72h, and
171 then rinsed five times with Milli-Q water. Bottles were then filled with 10% HCl (Baker instra-
172 analyzed) by volume and soaked for a minimum of one week, rotated, and soaked for another
173 week. Bottles were then rinsed five times with dilute acid (HCl, pH 2) and stored double-bagged
174 in plastic zip bags. All cleaning work was conducted in a Class 100 clean room.

175 **2.3 Analyses of total dissolved Cd and Zn using isotope dilution**

176 Samples for the analysis of total dissolved Zn, Cd, Fe, Mn, Cu and Ni concentrations
177 were collected shipboard by pressure-filtering X-Niskin bottles through an acid-washed 142mm,
178 0.2µM Supor membrane filter (Pall) within 3 hours of rosette recovery using high purity



179 (99.999%) N₂ gas. Total dissolved water samples were collected into 250 mL TMC polyethylene
180 bottles and were stored double-bagged in plastic zip bags. Seawater samples for ¹¹⁰Cd and ⁶⁷Zn
181 stable isotope uptake experiments were collected in the same way but without filtering. All
182 sample collection occurred shipboard within a TMC van containing laminar flow hoods and
183 plastic sheeting. Samples for total dissolved metal analysis were acidified to pH 1.7 with high
184 purity HCl (Optima, Fisher Scientific) within 7 months of sampling and were stored acidified at
185 room temperature for over 1 year prior to analysis.

186 Quantification of dissolved metals in samples and reference seawater was performed for
187 total dissolved Fe, Ni, Cu, Zn, and Cd using isotope dilution. 15 mL of acidified seawater sample
188 was spiked with 50 µL of a stable isotope spike solution artificially enriched in ⁵⁷Fe, ⁶¹Ni, ⁶⁵Cu,
189 ⁶⁷Zn, and ¹¹⁰Cd. All stable isotopes were received in solid form (Oak Ridge National
190 Laboratory). Initial dissolution and all subsequent dilutions were made using concentrated nitric
191 acid (Optima, Fisher Scientific). Concentrations and ratios of isotopes for each metal in the spike
192 solution were verified by inductively coupled plasma mass spectrometry (ICP-MS) using a
193 multi-element standard curve (SPEX CertiPrep). The composition of the isotope spike addition
194 was made such that the target isotope ratios in the total, 15mL spiked sample would be ⁵⁷Fe/⁵⁶Fe
195 = 0.7, ⁶¹Ni/⁶⁰Ni = 0.5, ⁶⁵Cu/⁶³Cu = 1, ⁶⁷Zn/⁶⁶Zn = 0.7, and ¹¹⁰Cd/¹¹⁴Cd = 1 and were verified with
196 ICP-MS. These ratios were chosen to minimize the uncertainty introduced by error propagation
197 through the isotope dilution equation (Wu and Boyle 1998; Rudge et al. 2009; Tan et al. 2020).
198 The same spike solution was used to spike all samples from all depths. Because it is
199 monoisotopic, total dissolved Mn was calculated using a modified isotope dilution equation:

$$200 \text{ Mn (nM)} = \frac{^{55}\text{Mn}_{\text{spike}}(\text{cps})}{^{57}\text{Fe}_{\text{spike}}(\text{cps})} * ^{57}\text{Fe}_{\text{spike}}(\text{nM}) * ^{57}\text{Fe}_{\text{slope}}(\text{cps/ppb}) * \frac{1}{(^{55}\text{Mn}_{\text{slope}})(\text{cps/ppb})} \quad (1)$$



201 in which $^{55}\text{Mn}_{\text{spl}}$ and $^{57}\text{Fe}_{\text{spl}}$ refer to the blank corrected counts per second (cps) of ^{55}Mn and ^{57}Fe
202 in the spiked sample, ^{57}Fe spike is the concentration of ^{57}Fe spike, $^{57}\text{Fe}_{\text{slope}}$ is the slope of the
203 external standard calibration curve (SPEX curve) relating ^{57}Fe cps to ppb, and $^{55}\text{Mn}_{\text{slope}}$ is the
204 slope of the external calibration curve (SPEX curve) relating ^{55}Mn cps to ppb. Due to the
205 acidification of seawater prior to ICP-MS analysis, Mn ICP-MS measurements do not include
206 contributions from humic-type Mn(III)-ligand complexes (Oldham et al. 2021). Until the
207 inclusion of Mn(III) is resolved and intercalibrated, we report these Mn values as Mn(II) and
208 note that they are consistent with prior studies employing the same acidification technique
209 (Sedwick et al. 2000; Noble et al. 2013; Gerringa et al. 2020).

210 Preconcentration of spiked seawater samples for total dissolved metal analysis was
211 performed using the automated solid phase extraction system seaFAST-pico (Elemental
212 Scientific) in offline concentration mode with an initial volume of 15 mL and elution volume of
213 500 μL (Bown et al. 2017; Rapp et al. 2017; Jackson et al. 2018; Wuttig et al. 2019). The
214 seaFAST contains a Nobias-chelate PA1 resin column (ethylenediaminetriacete and
215 iminodiacetate) suitable for the simultaneous preconcentration of several trace metals (Fe, Mn,
216 Zn, Cu, Co, Cd, Ni) with high sensitivity and quantitative recovery (Sohrin et al. 2008; Biller and
217 Bruland 2012). Adjusted seaFAST software settings were a 17 second load loop time and a
218 single 10 mL load cycle. Process blanks consisted of pH 2 HCl (Optima, Fisher Scientific) and
219 were processed as samples to account for any contamination introduced by instrument
220 processing.

221 Reagents consisted of a 1.5M ammonium acetate pH 6.0 buffer made using glacial acetic
222 acid and ammonium hydroxide (20-22%) of the highest purity (Optima, Fisher Chemical), a 1%
223 nitric acid rinse solution (Optima grade, Fisher Chemical), and a 10% nitric acid elution buffer

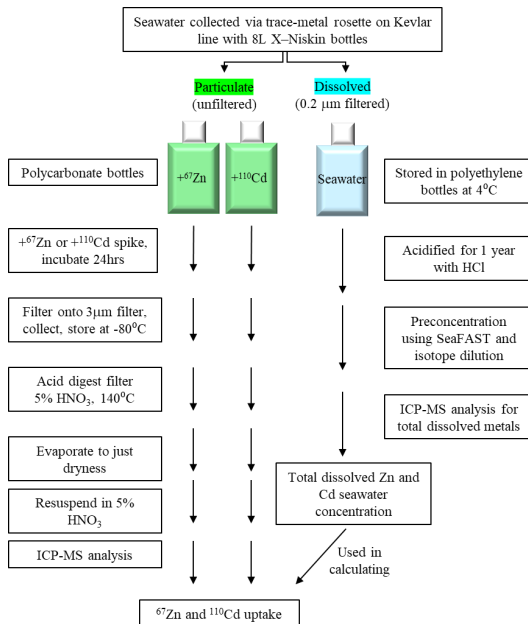


224 (Optima grade, Fisher Chemical) with 10 ppb indium (^{115}In , SPEX CertiPrep) added as an
225 internal standard. Solutions were prepared with $18.2\ \Omega$ Milli-Q water (Millipore). Polypropylene
226 15 mL centrifuge tubes used in sample processing were cleaned of potential metal contamination
227 by soaking in 10% HCl for 5 days and rinsing with pH 2 HCl prior to use.

228 Following offline seaFAST preconcentration, multi-elemental quantitative analysis was
229 performed using an iCAP-Q inductively coupled plasma-mass spectrometer (Thermo Scientific).
230 To minimize oxide interference on metal isotopes, a cooled spray chamber and helium collision
231 gas were employed. Analytes were measured in single quadrupole mode (kinetic energy
232 discrimination [KED]). Concentrations of Mn, Fe, Ni, Cu, Zn and Cd were determined using a
233 six-point external standard curve of a multi-element standard (SPEX CertiPrep), diluted to range
234 from 1-10 ppb in 5% nitric acid. An indium standard (SPEX CertiPrep) was similarly added to
235 these standard stocks, diluted to range 1-10 ppb. Instrument injection blanks consisted of 5%
236 nitric acid in Milli-Q. Standard curve R^2 values were ≥ 0.98 for all metals monitored. Method
237 accuracy and precision were assessed using the 2009 GEOTRACES coastal surface seawater
238 (GSC) standard ($n = 8$; **Table S3**), which produced values consistent with consensus results.

239 **2.4 Uptake experiments: ^{67}Zn and ^{110}Cd spiking, incubation, and sample collection**

240 ^{67}Zn and ^{110}Cd and stable isotope uptake experiments were modeled after those
241 conducted by Cox et. al. 2014, with the addition of Zn uptake measurements. An overall
242 schematic detailing these experiment workflows is shown in **Fig. 2**.



243

244 **Figure 2.** Diagram showing the overall workflow used to measure particulate uptake of ^{110}Cd
245 and ^{67}Zn and total dissolved Cd and Zn, after Cox et al. 2014.
246

247 Uptake experiments were performed at 18 stations total (Fig. 1). Raw (unfiltered)
248 seawater was collected shipboard over a depth range of 10 – 600 m into 250 mL TMC
249 polycarbonate incubation bottles. All incubation bottles were filled with minimal headspace such
250 that the total culture volume was ~275 mL. Two incubation bottles per depth were filled with
251 raw seawater— one was spiked with ^{67}Zn , the other was spiked with ^{110}Cd . The Cd and Zn
252 isotope spikes were prepared by dissolving ^{110}CdO and ^{67}ZnO (Oak Ridge National Laboratory)
253 in 5% HNO_3 (Seastar Baseline) and were diluted using Milli-Q water to minimize added acidity.
254 When added to the filled incubation bottles, the total added (spiked) concentration of Cd was 300
255 pM and the total added concentration of Zn was 2 nM. The chosen total added concentrations
256 were based on the surface ratio of total dissolved Cd (dCd) to total dissolved Zn (dZn) reported
257 previously for the Ross Sea (Fitzwater et al. 2000). Immediately after spiking, incubation bottles



258 were sealed, inverted to mix, and transferred to flow-through on-deck incubators for 24hr.

259 Incubators were shielded by black net neutral density screening to allow 20% ambient light
260 penetration.

261 Biomass was collected after 24hr by vacuum filtering the entire volume of each
262 incubation sample at 34.5 kPa (5 psi) onto an acid-cleaned 3µm, 50mm acrylic copolymer
263 (Versapore) filter (Pall) mounted on an acid-cleaned Teflon (Savillex) filtration rig. Samples
264 were filtered through 3 µm pore-size filters rather than 0.2 µm in order to minimize filtration
265 time (and thus time exposed to potential contamination) and to capture the bulk of eukaryotic
266 phytoplankton biomass typically found in the Southern Ocean. An aliquot of 1 mL of 0.2 µm
267 filtered surface seawater (collected at 10 m depth) was used to rinse the sample before collecting
268 the filter into an acid-cleaned 2 mL cryovial using acid-rinsed plastic forceps. Filter blanks were
269 duplicate 3 µm acid-clean Versapore (Pall) filters that were placed onto the filtration rig, rinsed
270 with filtered surface seawater, collected, stored, and processed as samples were to correct for any
271 contaminating metals present on the filters themselves. Blanks were collected at each station.
272 Filters were stored frozen at -80 °C in acid-cleaned cryovials until analysis. The filtration rig was
273 rinsed with pH 2 HCl between samples. Polycarbonate incubation bottles were cleaned between
274 stations with a 10% HCl rinse and several rinses in Milli-Q water, followed by a brief soak in
275 10% HCl followed by a pH 2 HCl rinse. All spike addition and sample filtration procedures were
276 completed in a fabricated shipboard positive-pressure clean room environment made of laminar
277 flow hoods and plastic sheeting.

278 We note that the total Zn and Cd uptake rate values presented in this study represent
279 potential uptake rates rather than true uptake rates—this naturally arises as a consequence of
280 adding the spiked tracer ^{67}Zn and ^{110}Cd into raw surface seawater. As this seawater is naturally



281 depleted in both metals, the spike addition artificially increases the total Zn and Cd present and
282 thus could perturb the response of biology to these additions. It should also be noted that both
283 ^{67}Zn and ^{110}Cd spikes were not equilibrated with natural seawater before their addition to
284 incubation bottles to maintain experimental consistency. Experiments of this nature have been
285 conducted previously using radioisotopes as tracers (Morel et al. 1994; Sunda and Huntsman
286 1995; Cullen et al. 1999; Hutchins et al. 1999), though we chose to use stable isotopes for ease of
287 shipboard use and waste disposal.

288 **2.5 Filter digestion and particulate ICP-MS analysis**

289 All work was performed in a Class 100 clean room under laminar flow hoods. Sample
290 filters were retrieved from storage at -80 °C, removed from cryovials using plastic acid-washed
291 forceps, and transferred into trace metal clean 15 mL PFA vials with 4 mL of 5% HNO₃
292 (Optima) containing a 1 ppb Indium (In) internal standard. Filters were digested for ~3.5h at 140
293 °C using a HotBlock® heating block (Environmental Express, USA). Filters were then removed
294 and discarded, leaving behind the liquid extract. After evaporating the remaining solution to just
295 dryness, the residue was resuspended in 2 mL of 5% HNO₃ (Optima) by light vortexing. Process
296 blank filters were digested and processed as sample filters were. Digests were analyzed in
297 duplicate by ICP-MS using a Thermo ICAP-Q plasma mass spectrometer calibrated to a multi-
298 element standard curve (Spex Certiprep) over a range of 1 – 20 ppb. Natural Cd and Zn isotope
299 abundances of the standards were assumed to calculate concentrations of ^{110}Cd , ^{111}Cd , ^{114}Cd ,
300 ^{67}Zn , ^{66}Zn , and ^{68}Zn . Digests were analyzed in KED mode after an 85s sample uptake window
301 and element mass windows were scanned 3 times during measurements. The 1 ppb In internal
302 standard was used to correct for variation in sample delivery and plasma suppression between
303 samples. Process blanks were subtracted from measured sample concentrations. Phosphorus



304 concentrations were simultaneously measured by ICP-MS and were calibrated to a standard
305 curve ranging from 100 – 3,200 ppb using a 1 ppm certified P stock (Alfa Aesar Specpure).
306 Equation #2 was used for the calculations described above:

$$M_{\text{particulate}} = \left[\frac{M_{\text{sample}}}{In_{\text{sample}}} - \frac{M_{\text{blank}}}{In_{\text{blank}}} \right] * \frac{In_{\text{digestion}}}{M_{\text{slope}}} * \frac{V_{\text{digested}}}{V_{\text{filtered}}} \quad (2)$$

307
308 where V_{filtered} is the total spiked sample volume estimated to have passed through the filter (275
309 mL), V_{digested} is the final volume the sample was resuspended in (2.0 mL), M_{sample} is the metal of
310 interest measured in the sample in units of counts per second (cps), M_{blank} is the metal of interest
311 measured in the process blanks (cps), M_{slope} is the slope of the metal of interest obtained by the
312 standard curve (cps ppb⁻¹), In_{sample} is the In measured in the sample (cps), In_{blank} is the In
313 measured in the process blanks (cps), $In_{\text{digestion}}$ is the cps of In measured in the 5% HNO₃+1 ppb
314 In digestion solution, and the calculated concentration of the metal of interest ($M_{\text{particulate}}$) is in
315 ppb (μg L⁻¹). This equation is the same as that used by Noble et. al. 2013 for the determination
316 of particulate metal concentrations using ICP-MS (Noble et al. 2013).

317 The Zn spike and Cd spike were also analyzed by ICP-MS using a tenfold dilution of
318 spike solution into 5% HNO₃ containing 1 ppb In to determine isotopic compositions and
319 concentrations. When added to filled incubation bottles (275 mL total volume), the added
320 concentrations were 288 pM ¹¹⁰Cd, 4.51 pM ¹¹¹Cd, and 1.69 pM ¹¹⁴Cd for Cd spiked bottles, and
321 were 1.91 nM ⁶⁷Zn, 0.045 nM ⁶⁶Zn, and 0.047 nM ⁶⁸Zn for Zn spiked bottles (**Table S2**). For all
322 stations and all depths, ⁶⁷Zn and ¹¹⁰Cd spike concentrations exceeded natural dissolved ⁶⁷Zn and
323 ¹¹⁰Cd concentrations, estimated by multiplying the total dissolved Zn and Cd by the natural
324 isotope abundance of ⁶⁷Zn and ¹¹⁰Cd (0.0410 and 0.1249, respectively; see comparisons in **Fig.**
325 **S2**).

326 **2.6 Calculating zinc and cadmium uptake using ⁶⁷Zn and ¹¹⁰Cd**



327 Total Zn and Cd uptake was calculated using Eq. (3) and Eq. (4), respectively. $^{110}\text{Cd}_{\text{Sample}}$
328 and $^{67}\text{Zn}_{\text{Sample}}$ are the particulate ^{110}Cd and ^{67}Zn measured by ICP-MS analysis of the $3\text{ }\mu\text{m}$
329 sample filter (using the digestion protocol described in the prior section) normalized to the total
330 culture volume (275 mL) and 24 hr of incubation. $^{110}\text{Cd}_{\text{Sample}}$ and $^{67}\text{Zn}_{\text{Sample}}$ already in the
331 particulate fraction (that is, the pCd and pZn that existed in the water column upon collection of
332 the raw seawater samples) were accounted for by subtracting these pre-existing particulate ^{110}Cd
333 and ^{67}Zn values, $^{110}\text{Cd}_{\text{PEP}}$ and $^{67}\text{Zn}_{\text{PEP}}$. The pre-existing particulate value for ^{110}Cd was obtained
334 from incubation bottles that had Zn added, but no Cd spike. Likewise, the pre-existing particulate
335 value for ^{67}Zn was obtained from incubation bottles that had Cd added, but no Zn spike. The
336 ^{67}Zn spike solution was confirmed to contain virtually no ^{110}Cd , ^{111}Cd , nor ^{114}Cd . The ^{110}Cd
337 spike was likewise confirmed to contain virtually no ^{67}Zn , ^{64}Zn , nor ^{66}Zn . As a result, we
338 assumed that the added ^{67}Zn spike did not affect the pre-existing Cd, nor did the ^{110}Cd spike
339 affect the pre-existing Zn. It is assumed that the pre-existing particulate blank was in steady
340 state, i.e. that it represented the Cd or Zn already in the particulate fraction and that any possible
341 natural uptake that could occur during incubation for 24 h was negligible. The total dissolved
342 pool of each metal isotope (denominator of each equation) is the sum of the dissolved ^{110}Cd or
343 ^{67}Zn added as the spike ($^{110}\text{Cd}_{\text{Spike}}$, $^{67}\text{Zn}_{\text{Spike}}$) plus the natural, pre-existing dissolved ^{110}Cd or ^{67}Zn
344 that was in the raw seawater ($^{110}\text{Cd}_{\text{Natural}}$, $^{67}\text{Zn}_{\text{Natural}}$) collected at each depth. To calculate
345 $^{110}\text{Cd}_{\text{Natural}}$ and $^{67}\text{Zn}_{\text{Natural}}$, the total dissolved Cd or Zn measured by isotope dilution-ICP-MS
346 (Cd_{Total} , Zn_{Total}) was multiplied by the natural abundance of ^{110}Cd and ^{67}Zn (12.49% and 4.10%,
347 respectively). Dividing the particulate ^{110}Cd and ^{67}Zn by the total dissolved ^{110}Cd and ^{67}Zn yields
348 the fraction of these metal isotopes that moved from the dissolved pool to the particulate pool per
349 day (equation 3 and equation 4, respectively):



350
$$\text{Cd}_{\text{total}} \text{ Uptake Rate (pmol L}^{-1} \text{ d}^{-1}\text{)} = \frac{[{}^{110}\text{Cd}_{\text{Sample}} \text{ (pmol L}^{-1} \text{ d}^{-1}\text{)} - {}^{110}\text{Cd}_{\text{PEP}} \text{ (pmol L}^{-1} \text{ d}^{-1}\text{)}]}{[{}^{110}\text{Cd}_{\text{Spike}} \text{ (pmol L}^{-1}\text{)} + {}^{110}\text{Cd}_{\text{Natural}} \text{ (pmol L}^{-1}\text{)}]} \times \text{Cd}_{\text{total}} \text{ (pmol L}^{-1}\text{)} \quad (3)$$

351
$$\text{Zn}_{\text{total}} \text{ Uptake Rate (pmol L}^{-1} \text{ d}^{-1}\text{)} = \frac{[{}^{67}\text{Zn}_{\text{Sample}} \text{ (pmol L}^{-1} \text{ d}^{-1}\text{)} - {}^{67}\text{Zn}_{\text{PEP}} \text{ (pmol L}^{-1} \text{ d}^{-1}\text{)}]}{[{}^{67}\text{Zn}_{\text{Spike}} \text{ (pmol L}^{-1}\text{)} + {}^{67}\text{Zn}_{\text{Natural}} \text{ (pmol L}^{-1}\text{)}]} \times \text{Zn}_{\text{total}} \text{ (pmol L}^{-1}\text{)} \quad (4)$$

352 **2.7 Nutrient analyses**

353 Seawater samples taken for macronutrient analysis were filtered through 0.2 μm Supor
354 (Pall) membrane filters and frozen at sea in acid-washed 60-mL high-density polyethylene
355 (HDPE) bottles until analysis. Nutrient analyses were conducted by nutrient autoanalyzer by Joe
356 Jennings at Oregon State University using previously described methods (Noble et al. 2012).

357 **2.8 Statistics and plotting**

358 Dissolved ecological stoichiometries were obtained from the slopes of two-way (type II)
359 least squares linear regressions performed using the script lsqfitma.m rewritten from MATLAB
360 to Python by Rebecca Chmiel (<https://github.com/rebecca-chmiel/GP15>). A correlation matrix of
361 various parameters measured during NBP18-01 was created with SciPy v1.5.2 using the
362 scipy.stats.pearsonr function, yielding Pearson correlation coefficients and p values that were
363 visually represented using Seaborn v.0.11.1 and Matplotlib v3.3.2. Ocean sections were plotted
364 using Ocean Data View v5.3.0 with gridded bathymetry file ETOPO1_2min. Outliers (see Data
365 Availability) were excluded from ocean sectional plots. Mixed layer depth was calculated using
366 the potential density function (pdem) within the python-seawater module (v3.3.4). Figures were
367 made using matplotlib (v3.3.2), Ocean Data View (v5.5.2), Excel (2019), and RStudio
368 (v1.3.1093). ODV color palettes (<https://doi.org/10.5281/zenodo.1243862>) are inverse ‘roma’ for
369 trace metal and macronutrient concentrations, ‘thermal’ for Zn and Cd uptake rates, and ‘algae’
370 for total fluorescence (Crameri 2023).

371 **3 Results**

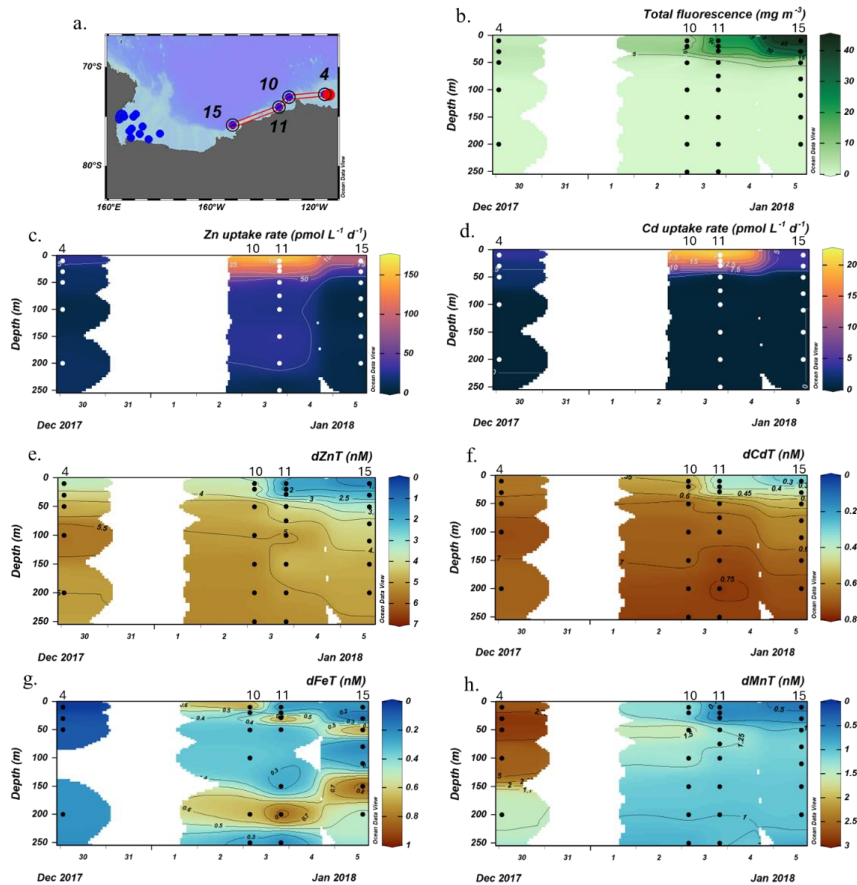
372 **3.1 Amundsen Sea**





373 Zn and Cd uptake rate experiments were conducted at 18 stations. We define 3 groups of
374 stations based on location: the Amundsen Sea, Ross Sea, and Terra Nova Bay (TNB) groups
375 (**Fig. 1**). Uptake rates were assessed at 3 stations (4, 11 and 15) within the Amundsen Sea group,
376 6 stations (20, 29, 32, 35, 62, and 67) within the Ross Sea group, and 9 stations (22, 27, 41, 46,
377 52, 57, 72, 76 and 79) within the TNB group spanning ~10 – 250 m depth for a total of 18
378 stations and 125 samples. An overall schematic detailing these experiment workflows is shown
379 in **Fig. 2**. The experimental design was validated by comparison of surface particulate ^{67}Zn : ^{68}Zn
380 and ^{110}Cd : ^{114}Cd ratios measured in spiked samples with those measured in control (unspiked)
381 samples. Samples spiked with ^{67}Zn had particulate ^{67}Zn : ^{68}Zn ratios larger than natural abundance
382 ratios at all stations (as was also true for ^{110}Cd spiked samples and Cd natural abundances; **Fig.**
383 **S1**), indicative of uptake of the spike into the particulate phase.

384 The Amundsen Sea stations represented a linear cruise track, and we report total
385 dissolved metal concentrations (dMetal_T) and uptake rates (ρMetal) over time in order of station
386 sampling date (**Fig. 3a**).



387

388 **Figure 3.** Total fluorescence and trace metal concentrations measured at Amundsen Sea stations
389 shown over time. (a) Map showing station locations, (b) total chlorophyll (Chl) fluorescence, (c)
390 total Zn uptake rates, (d) total Cd uptake rates, (e) total dissolved Zn, (f) total dissolved Cd, (g)
391 total dissolved Fe, and (h) total dissolved Mn measured in the upper 250 m represented in color
392 scale. Uptake experiments were not performed at station 10. Metal concentrations measured to
393 500 m depth are shown in Figure S3. dZnT, total dissolved Zn; dCdT, total dissolved Cd; dFeT,
394 total dissolved Fe; dMnT, total dissolved Mn.
395

396

Among these stations, total Chl fluorescence was lowest at station 4 and increased

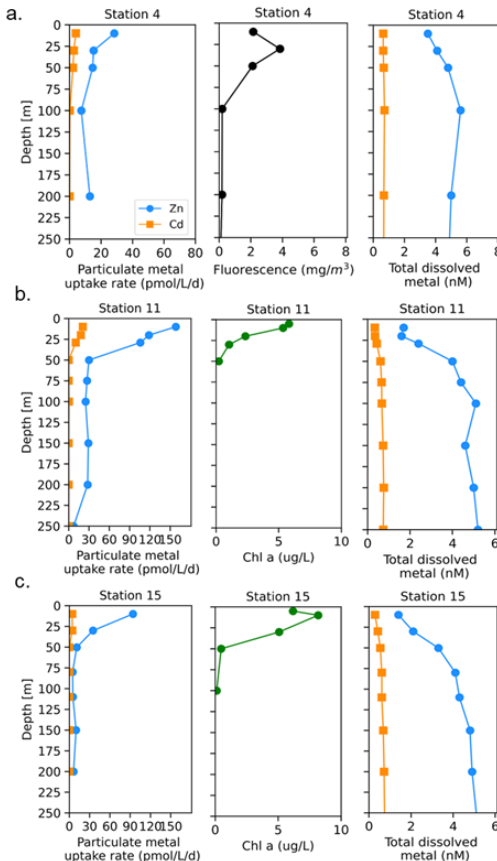
397 moving westward along the transect to a Chl maximum of 41.8 mg m^{-3} at station 15, 10 m (Fig.

398 **3b).** Maximum surface concentrations of dZn, dCd and dMn were highest at station 4 (3.5 nM,

399 639 pM, and 2.6 nM at 10 m, respectively; **Fig. 3e, f, h**), likely reflecting the relatively smaller



400 amount of total biomass (as indicated by total Chl fluorescence; **Fig. 3b**) at this station.
401 Concentrations of dZn, dCd and dMn decreased moving westward along the transect (**Fig. 3e, f,**
402 **h**) as total Chl fluorescence increased (**Fig. 3b**). Total Zn uptake rates (ρ_{Zn}) and total Cd uptake
403 rates (ρ_{Cd}) were highest at station 11 (158 and 21 pmol L⁻¹ d⁻¹, respectively, at 10 m; **Fig. 3c,d;**
404 **Fig. 4b**). Among the three Amundsen Sea stations, the largest movement of both Zn and Cd into
405 the particulate phase therefore occurred at station 11, concurrent with the relatively higher dFe_T
406 surface values observed at station 11 (0.2 nM dFe compared to 0.01 nM at station 4, 10 m; **Fig.**
407 **3g, Fig. S3c**). The dFe concentrations exceeding 1 nM near the seafloor are consistent with a
408 sedimentary or subglacial source (**Fig. S3c**). Overall, ρ_{Zn} and ρ_{Cd} profiles exhibited trends in
409 which values were highest within the upper 50 m at all three stations and decreased with depth,
410 following the trend in Chl a or total Chl fluorescence (**Fig. 4**). Vertical sections of dZn and dCd
411 through the water column mirrored these trends (**Fig. 4**), demonstrating the movement of these
412 dissolved metal micronutrients into the particulate phase.

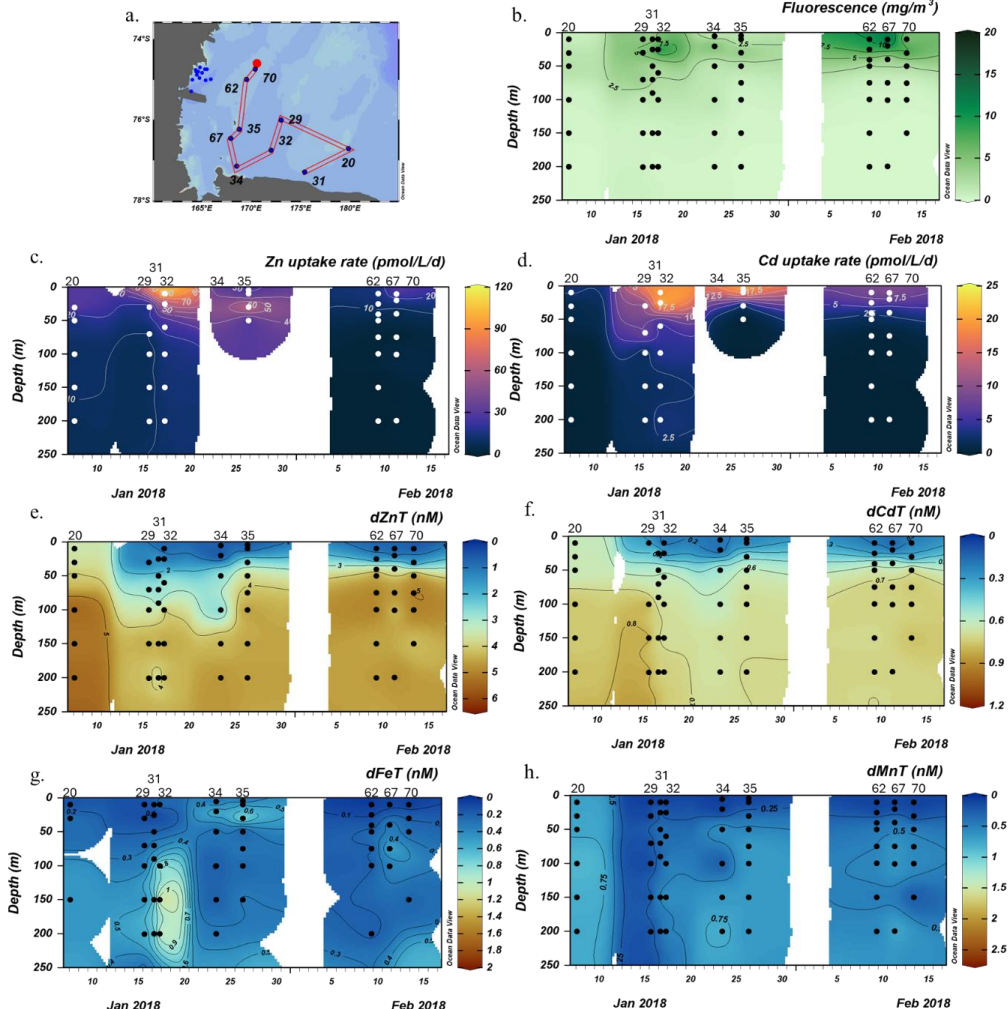


413

414 **Figure 4.** Depth profiles of total Zn and Cd uptake rates, total chlorophyll fluorescence (or
415 chlorophyll *a*) and total dissolved metal measured in the upper 250 m at (a) station 4, (b) station
416 11, and (c) station 15 sampled along the Amundsen Sea shelf. Total chlorophyll (Chl) fluorescence
417 is reported for stations where chlorophyll *a* (Chl *a*) data was not measured.
418

419 3.2 Ross Sea

420 We next investigated the dissolved Zn and Cd demand of the natural phytoplankton
421 community at stations sampled over the Ross Sea shelf. Data collected from this group is
422 presented over time, in order of sampling date (**Fig. 5**).
423



424

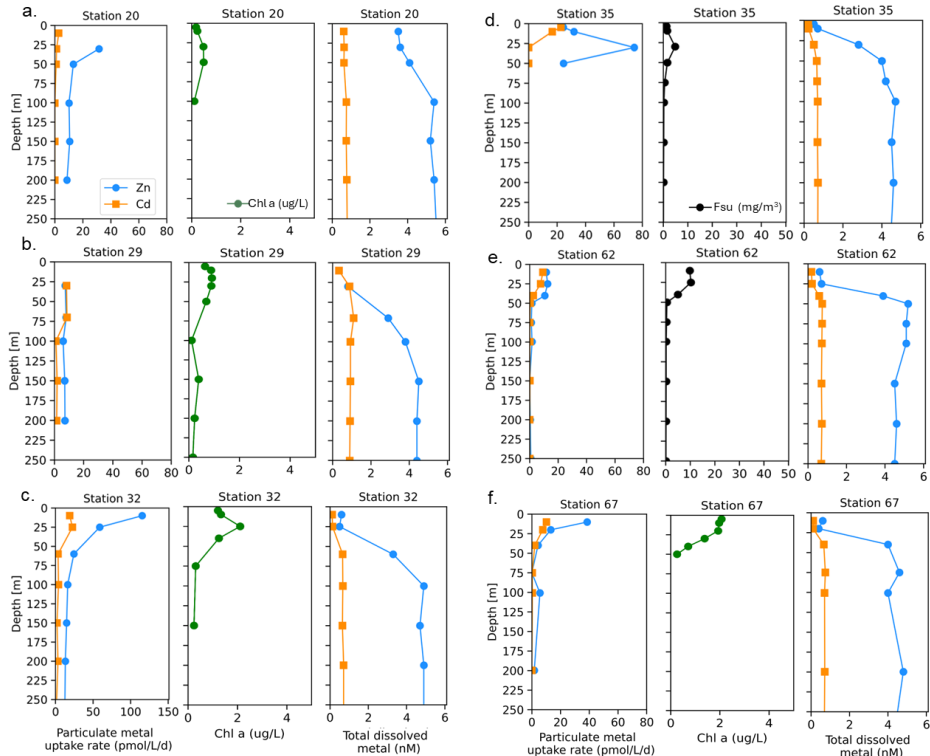
425 **Figure 5.** Total fluorescence and trace metal concentrations measured at Ross Sea stations
426 shown over a latitudinal transect. (a) Map showing station locations, (b) total chlorophyll (Chl)
427 fluorescence, (c) total Zn uptake rates, (d) total Cd uptake rates, (e) total dissolved Zn, (f) total
428 dissolved Cd, (g) total dissolved Fe, and (h) total dissolved Mn measured in the upper 250 m
429 represented in color scale. Uptake experiments were not performed at stations 31, 34, and 70.
430 Metal concentrations measured to 800 m depth are shown in Figure S4. dZnT, total dissolved Zn;
431 dCdT, total dissolved Cd; dFeT, total dissolved Fe; dMnT, total dissolved Mn.
432

433

434 We note that unlike the Amundsen Sea sector, the stations sampled in this group did not
follow a linear cruise track, thus we cannot make inferences regarding latitudinal or longitudinal



435 changes. Surface Chl fluorescence was highest at stations 32 and 67 with maximum values of
436 15.8 and 14.6 mg m⁻³ at 25 m and 10 m, respectively (**Fig. 5b**). With the exception of station 20,
437 dZn and dCd demonstrated high levels of surface depletion within the upper 25 m (**Fig. 5e,f**)
438 with average concentrations of 0.63 ± 0.13 nM and 0.19 ± 0.09 nM respectively at ≤ 10 m.
439 Compared to 100 m values (i.e., below the MLD), concentrations at 25 m were equivalent to
440 87%, 34%, 85%, 85%, 77%, and 88% decreases in dZn and 83%, 19%, 84%, 67%, 64%, and
441 75% decreases in dCd at stations 32, 20, 67, 35, 29, and 62, respectively. Measured dMn
442 concentrations were also highly depleted within the upper 250 m at all Ross Sea stations
443 (average 10 m dMn = 0.18 ± 0.26 nM; **Fig. 5h**). While dFe was depleted within the upper 10 m
444 at all stations (average dFe concentration at 10 m = 0.12 ± 0.12 nM), concentrations exceeding 1
445 nM were observed below 100 m at station 32 (**Fig. 5g**) and extended down to 650 m (**Fig. S4c**),
446 implying a sedimentary source. The largest Zn uptake rate measured among all stations in this
447 group ($115 \text{ pmol L}^{-1} \text{ d}^{-1}$) was observed at station 32, 10 m (**Fig. 6c**). As observed in the
448 Amundsen Sea, ρ Zn, ρ Cd and total Chl a or Chl fluorescence profiles exhibited surface maxima
449 and became depleted with depth and were again mirrored by nutrient-like dZn and dCd depth
450 profiles (**Fig. 6**), indicative of uptake of these metals into the particulate phase in surface waters.



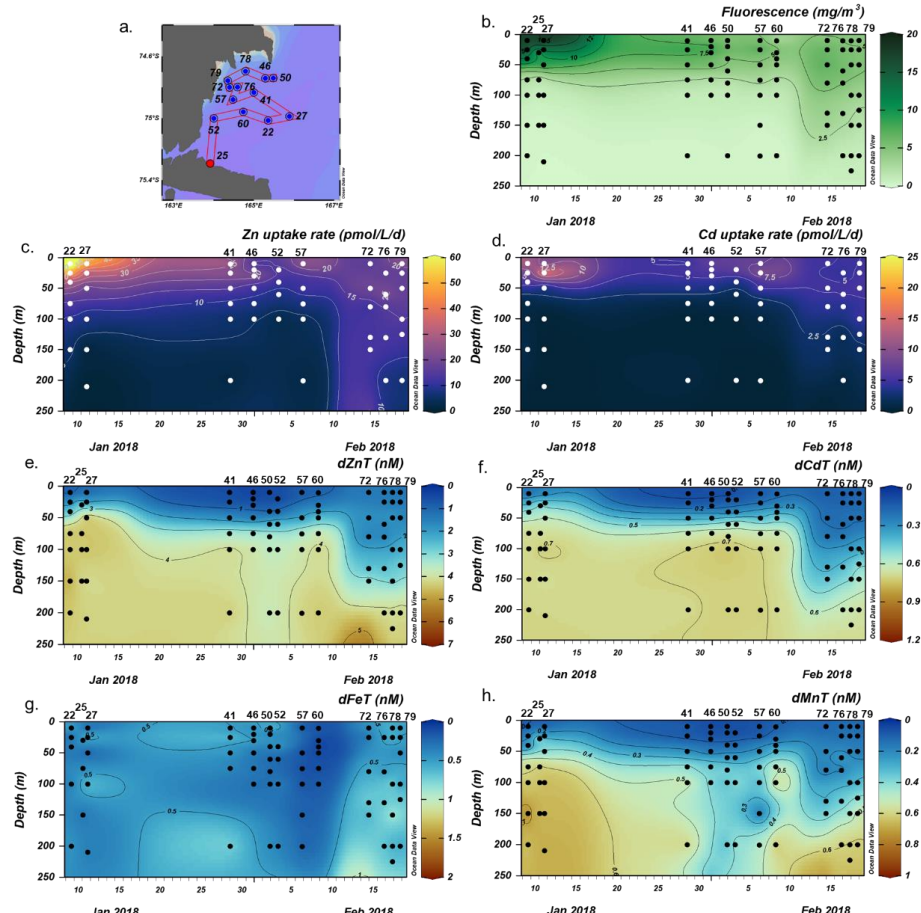
451

452 **Figure 6.** Depth profiles of total Zn and Cd uptake rates, total chlorophyll fluorescence (or,
453 where available chlorophyll a), and total dissolved metal ($dMetal_T$) measured in the upper 250 m
454 at (a) station 20, (b) station 29, (c) station 32, (d) station 35, (e) station 62, and (f) station 67
455 sampled along the Ross Sea shelf. Total chlorophyll (Chl) fluorescence is reported for stations
456 where chlorophyll a (Chl a) data were not measured.

457

458 3.3 Terra Nova Bay

459 Zinc and Cd uptake rate data collected from stations sampled in Terra Nova Bay (TNB)
460 were visualized over time due to repeated sampling within a small geographic region and similar
461 timeframe (Fig. 7a). This allowed for an analysis of how dissolved metal concentrations and
462 metal uptake rates changed throughout January–February 2018 within the same spatial area.
463 Station data is presented in order of sampling date, from the earliest (station 22, sampled in early
464 January) to the latest (station 79, sampled in late February).



465
466

467 **Figure 7.** Total fluorescence and trace metal concentrations measured at Terra Nova Bay (TNB)
468 stations shown over time. (a) Map showing station locations, (b) total chlorophyll (Chl)
469 fluorescence, (c) total Zn uptake rates, (d) total Cd uptake rates, (e) total dissolved Zn, (f) total
470 dissolved Cd, (g) total dissolved Fe, and (h) total dissolved Mn measured in the upper 250 m
471 represented in color scale. Uptake experiments were not performed at stations 70 and 34. Metal
472 concentrations measured to 600 m depth are shown in Figure S5. dZnT, total dissolved Zn;
473 dCdT, total dissolved Cd; dFeT, total dissolved Fe; dMnT, total dissolved Mn.
474

475 Surface Chl fluorescence was highest in early January ($\sim 18 \text{ mg m}^{-3}$) and waned into
476 February (Fig. 7b), similar to observed trends in Zn and Cd uptake rates (Fig. 7 c,d). Of all TNB
477 stations, stations 22 and 27, sampled in January, had the highest maximum Zn uptake rates of
478 $89.9 \text{ pmol L}^{-1} \text{ d}^{-1}$ and $46.0 \text{ pmol L}^{-1} \text{ d}^{-1}$, respectively, at 10 m (Fig. 8a,b). Cd uptake rates were



479 also highest at these stations with values of $13.4 \text{ pmol L}^{-1} \text{ d}^{-1}$ and $20.1 \text{ pmol L}^{-1} \text{ d}^{-1}$ (**Fig. 8a,b**).

480 At the final station (station 79, sampled in late February) maximum uptake rates of both metals

481 had sharply decreased to $24.7 \text{ pmol Zn L}^{-1} \text{ d}^{-1}$ and $5.0 \text{ pmol Cd L}^{-1} \text{ d}^{-1}$ (**Fig. 8i**). Overall,

482 maximum uptake rates of both metals decreased over time within TNB (**Fig. 7c,d**), consistent

483 with the decrease in total Chl fluorescence (**Fig. 7b**) likely due to the aging and decline of the

484 phytoplankton bloom.

485 Surface depletion of dZn, dCd, and dMn was observed at all stations with average

486 dissolved concentrations of $0.82 \pm 0.47 \text{ nM}$ Zn, $0.13 \pm 0.06 \text{ nM}$ Cd, and $0.08 \pm 0.04 \text{ nM}$ Mn at

487 10 m depth (**Fig. 7e,f,h**). Notably, increased surface concentrations of dZn, dCd, and dMn were

488 apparent at the late stations 72, 76, 78 and 79, with dZn $\sim 2 \text{ nM}$, dCd $\sim 300 \text{ pM}$, and dMn ~ 0.2

489 nM (**Fig. 7e,f,h; Fig. S5**). Dissolved macronutrient (phosphate, nitrate and nitrite, and silicate)

490 concentrations also followed this trend, with increased surface concentrations at the late stations

491 (**Fig. S6**). As with the Amundsen and Ross Sea station groups, Zn and Cd uptake rates within

492 TNB tended to be highest at the surface $\leq 50 \text{ m}$ as also observed in total Chl fluorescence trends

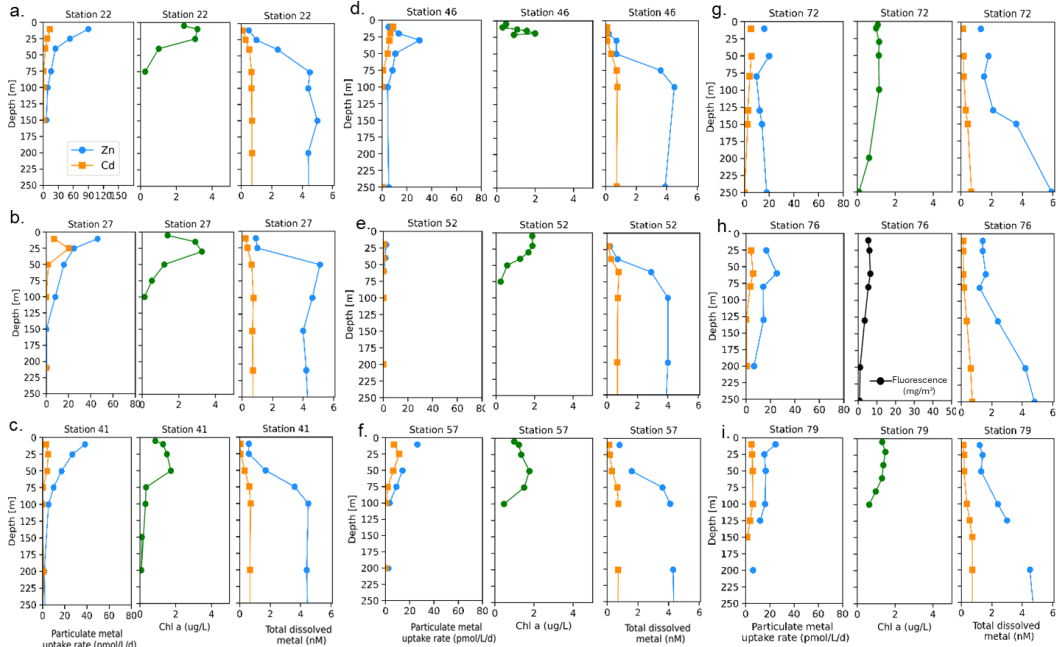
493 and mirrored the decrease in total dissolved Zn and Cd (**Fig. 8**). Unlike the Amundsen and Ross

494 Sea stations, where Cd uptake consistently became negligible ($\sim 0 \text{ pM L}^{-1} \text{ d}^{-1}$) by 100 m (**Fig. 4**;

495 **Fig. 6**), measurable Cd uptake persisted in TNB to 150 m at stations 72 and 79 (**Fig. 8g,i**).

496 Measurable Zn uptake rates were also captured at deeper depths at these late TNB stations (**Fig.**

497 **8g,h,i**).



498

499 **Figure 8.** Depth profiles of total Zn and Cd uptake rates, total chlorophyll fluorescence (or,
500 where available, chlorophyll a), and total dissolved metal (dMetalT) measured in the upper 250
501 m at (a) station 22, (b) station 27, (c) station 41, (d) station 45, (e) station 52, (f) station 57, (g)
502 station 72, (h) station 76, and (i) station 79 within Terra Nova Bay. Total chlorophyll (Chl)
503 fluorescence is reported for stations where chlorophyll a (Chl a) data was not measured.
504

505

The increased surface concentrations of dZn and dCd and macronutrients, as well as the

506 persistence of measurable uptake rates at deeper depths, at these late TNB stations may be

507 attributed to the deepening of the mixed layer (**Fig. S7**). Vertical mixing was evidenced by more

508 uniform potential densities, temperatures, dissolved oxygen (O_2) concentrations, salinity, and

509 beam transmission measurements at the late TNB stations within the upper 200 m (**Fig. S7**).

510 Higher (>0.5 nM) dFe concentrations were also observed below 100 m at these late stations (**Fig.**

511 **7g**) and increased with depth (>2 nM), as did dZn and dMn concentrations, possibly due to

512 sedimentary inputs (Giordano et al. 1999) (**Fig. S5**). At these late stations (Station 76, 78, 79)

513 mixing replenished surface concentrations of both macronutrients (**Fig. S6**) and dZn (**Fig. S5a**),

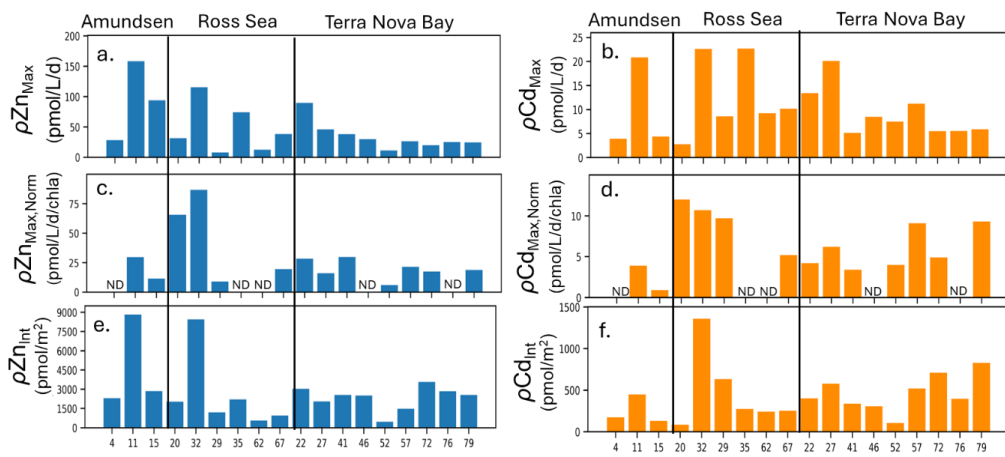


514 but dZn was replenished to a lower extent. For example, comparing 50 m “replenished” surface
515 values of P, N+N, and Si to deepwater (200 m) values at Station 79, percent changes from deep
516 to surface values were -0.35% for P, -0.30% for N+N, and -0.26% for Si (a % change of 0 would
517 indicate complete replenishment; i.e, if values at 200 m and at 50 m were equal). In contrast, the
518 percent change from deep (200m) to surface (50m) dZn at Stn79 was lower, -0.71%. Hence, dZn
519 was apparently replenished to a lesser extent compared to macronutrients, which may reflect a
520 sustained high demand for Zn generating a dearth of this micronutrient despite macronutrient
521 replenishment.

522 **4 Discussion**

523 **4.1 Overview of Zn and Cd uptake at 18 stations**

524 Maximum Zn and Cd uptake rates observed at each station (all of which were observed at
525 ≤ 10 m depth; **Fig. 9a,b**) with uptake rates normalized to Chl a ($\mu\text{g/L}$) as a proxy for biomass
526 (**Fig. 9c,d**).



527
528 **Figure 9.** Unnormalized (a) maximum Zn uptake rates (ρZn_{Max}) and (b) maximum Cd uptake
529 rates (ρCd_{Max}) at each station grouped by area (Amundsen Sea, Ross Sea, Terra Nova Bay). (c)
530 ρZn_{Max} and (d) ρCd_{Max} normalized to chlorophyll a ($\mu\text{g L}^{-1}$) measured at each station. (e) Depth
531 integrated (10 m-250 m) ρZn and ρCd values at each station. ND, no data (chlorophyll a not
532 measured).





533 Overall, high ($>25 \text{ pmol L}^{-1} \text{ d}^{-1} \text{ Chl a (ug/L)}^{-1}$) Chl a-normalized Zn uptake rates were measured
534 at station 11 in the Amundsen Sea and at stations 20 and 32 in the Ross Sea (**Fig. 9c**). The
535 highest Chl a-normalized Cd uptake rates among all 18 stations were also measured at stations
536 20 and 32 (**Fig. 9d**). Across TNB, Chl a-normalized maximum Zn and Cd uptake ranged from
537 $6.0 - 28.3 \text{ pmol L}^{-1} \text{ d}^{-1} \text{ Chl a}^{-1}$ for Zn, and $3.4 - 9.3 \text{ pmol L}^{-1} \text{ d}^{-1} \text{ Chl a}^{-1}$ for Cd; **Fig. 9c,d**).
538 Integrated (10 m-250 m) uptake rate values were highest for Zn at stations 11 and 32, and highest
539 for Cd at station 32 (**Fig. 9e,f**). Increases in integrated Cd and Zn uptake at the late stations 72,
540 76 and 79 reflected the deeper depths to which uptake rates of these metals remained measurable,
541 likely reflecting deepened mixed layers (**Fig. S7**) and/or sinking of the phytoplankton
542 community, as seen in the fluorescence data to beyond 150m depth (**Fig. 7b**). The presence of
543 Chl a (**Fig. 8g,i**) implies these deep phytoplankton communities may still be alive, if not actively
544 photosynthesizing. We previously identified ZCRP-B, a membrane-associated protein involved
545 in high-affinity Zn transport (Kellogg et al. 2022). These proteins have a single transmembrane
546 domain, implying function as a membrane-tethered ligand to assist in the acquisition of Zn from
547 seawater in cooperation with adjacent zinc transporters (ZIP transporters). Hence ZCRP-B could
548 be a potential site of Zn binding and ‘uptake’, as our uptake rate measurements do not discern
549 between extracellular and intracellular Zn, even if the phytoplankton are inactive due to a lack of
550 photosynthetic energy at these depths.

551 **4.2 Use of metal uptake rates to determine depletion timeframes**

552 The measurement of total dissolved metal concentrations over large latitudinal or
553 longitudinal areas allows for the characterization of metal inventories, though these are snapshots
554 of inventories observed at specific times. The measurement of metal uptake rates allows us to
555 gain new insight into how these inventories came to be and the timeframes over which they are



556 consumed and replenished. Due to the resetting of surface dissolved metal concentrations to
557 those of deepwater values during austral winter with deep winter mixing, the Ross Sea of the
558 Southern Ocean is particularly applicable to this type of timeframe study (Sedwick and DiTullio
559 1997; Sedwick et al. 2011).

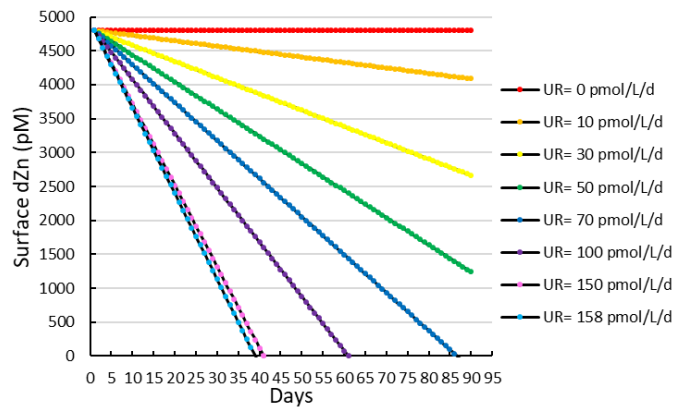
560 Using the Zn uptake rates measured in this study, we can estimate the time required for
561 the high levels of primary production observed in the Southern Ocean to draw down surface dZn
562 from high (deep water) winter concentrations to the surface concentrations observed during
563 austral summer 2017. The Southern Ocean growing season typically spans October-March, with
564 primary productivity peaking November-January and the area of open (ice-free) water over the
565 Ross Sea shelf linearly increasing from November-mid January (Sedwick et al. 2011). Vertical
566 profiles of nutrients and micronutrients in coastal Antarctic ecosystems such as the Ross Sea are
567 reset and become uniform with depth during the winter months due to whole-water column
568 mixing and an absence of photosynthetic activity during the dark winter under the sea ice (Noble
569 et al. 2013). As a result, the drawdown of nutrients in the upper water column observed during
570 the spring and summer seasons is the result of less than one year's biological influence. For this
571 simple calculation, we ignore the upward flux of Zn (upwelling = 0) and assume a high export
572 ratio of 0.8 due to bloom productivity being dominated by diatoms and *Phaeocystis antarctica*,
573 both of which sink rapidly and thus contribute substantially to carbon export flux (Asper and
574 Smith 1999; DiTullio et al. 2000). The depletion of dZn from a surface box was therefore
575 estimated as:

$$576 \left(\frac{dZn}{dt} \right)_{\text{surface box}} = -\rho Zn + (Rf * \rho Zn) + \text{upwelling}$$

577 Where Rf is the remineralization factor equal to 1 - export ratio.



578 Taking station 11, for which the highest Zn uptake rate was observed, as an extreme case:
579 with a maximum Zn uptake rate of $158 \text{ pmol L}^{-1} \text{ d}^{-1}$, it would take only 25 days to deplete a
580 surface winter concentration of 4.8 nM (that is, the average deepwater ($< 200 \text{ m}$) dZn
581 concentration for all stations measured in this study) down to the observed surface concentration
582 of 1.7 nM at station 11, assuming a constant uptake rate and no additional inputs of dissolved Zn
583 (**Fig. 10**).



584 **Figure 10.** A simple model estimating the time (in days) required to deplete the estimated
585 average winter surface concentration of dZn (4.8 nM) over a range of various Zn uptake rates
586 (UR). 158 pmol/L/d was the maximum Zn uptake rate observed in this study (station 11, 10 m).
587
588

589 Given that dZn surface depletion to sub-nanomolar levels was observed throughout much
590 of the CICLOPS expedition, prolonged high levels of Zn uptake and export that overwhelm
591 replenishment by vertical mixing and/or remineralization are likely key to giving rise to the
592 observed extent of seasonal surface dZn depletion. These calculations were conducted as a proof-
593 of-concept to determine if uptake rates were sufficient to draw down the otherwise abundant dZn
594 inventory on seasonal timescales. Future studies could conduct mesoscale modeling of the
595 region, replacing upwelling including eddy diffusion and advection. Notably, any dZn upwelling

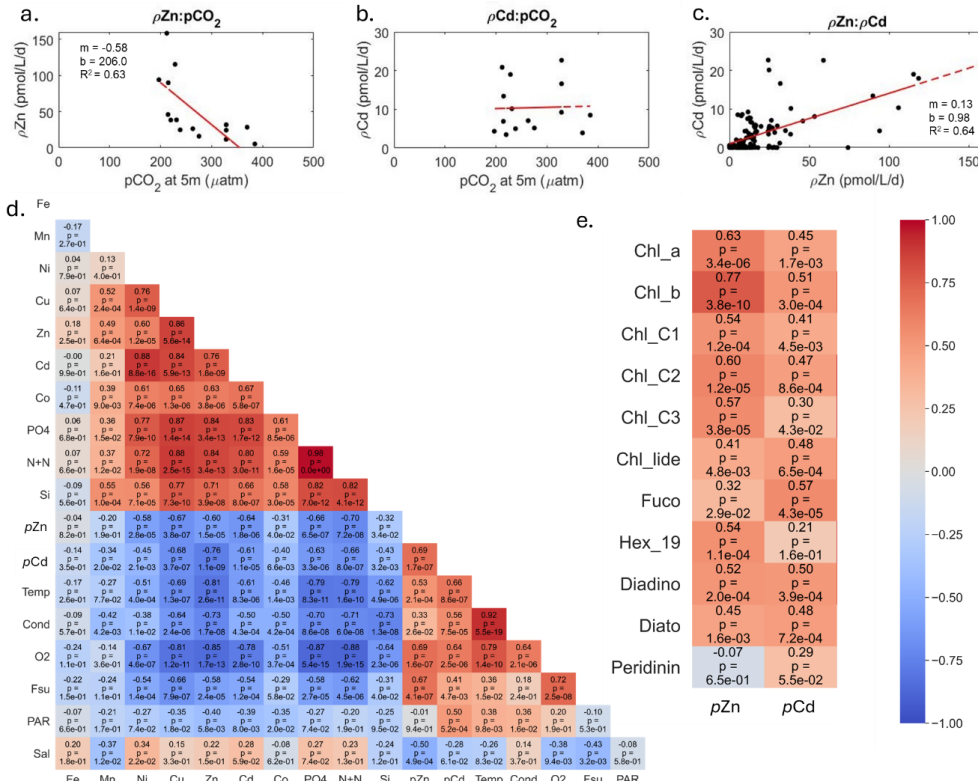


596 flux into the euphotic zone would require even higher Zn uptake rates to create the seasonal
597 surface Zn depletion we observed on this expedition.

598

599 **4.3 Influences on Zn and Cd uptake**

600 We next consider the factors driving the magnitude of ρ_{Zn} and ρ_{Cd} . As noted above, ρ_{Zn}
601 and ρ_{Cd} were positively correlated with total Chl fluorescence or Chl a at every station (**Fig. 4**;
602 **Fig. 6**; **Fig. 8**), demonstrating the influence of total autotrophic biomass on uptake rates. A
603 Pearson correlation analysis comparing the abundance of individual algal pigments to ρ_{Zn} and
604 ρ_{Cd} throughout the water column for all stations revealed significant, positive correlations
605 (Pearson correlation coefficient > 0.50 , $p \leq 1.2\text{e-}4$) between ρ_{Zn} and Chl a, Chl b, and Chl c1, c2
606 and c3. Pearson correlation coefficients are normally symbolized as rho (ρ), but to avoid
607 confusion with our uptake symbol (ρ), and with p-values (p), they are herein referred to as 'cc'
608 values. The correlation between ρ_{Zn} and Chl b was strongest ($\text{cc} = 0.77$, $p = 3.8\text{e-}10$) of any
609 pigment (**Fig. 11e**).



610

611 **Figure 11.** Relationships comparing seawater CO_2 partial pressure ($p\text{CO}_2$) at 5 m depth to (a) Zn
612 uptake rates (ρZn ; $n=15$, $R^2 = 0.63$) and (b) Cd uptake rates (ρCd ; $n=15$) measured at surface
613 (≤ 10 m) depths. (c) Relationship between ρZn and ρCd for all depths ($n=121$, $R^2 = 0.64$). (d)
614 Visual representation of the correlation matrix comparing all water column parameters measured
615 with depth with warm and cool colors indicative of positive and inverse correlations,
616 respectively. Pearson correlation coefficients and p values are shown. (e) Representation of the
617 correlation matrix comparing ρZn and ρCd to various phytoplankton pigments. Fe, Mn, Ni, Cu,
618 Zn, Cd, and Co labels correspond to total dissolved metal concentrations. PO4, N+N, and Si
619 correspond to total dissolved concentrations of phosphate, the sum of nitrate+nitrite, and silicate.
620 Temp, temperature; cond, conductivity; O2, dissolved oxygen; Fsu, total fluorescence; PAR,
621 photosynthetically active radiation; Sal, salinity. Chl_a, chlorophyll a; Chl_b, chlorophyll b;
622 Chl_c1, chlorophyll c1; Chl_c2, chlorophyll c2; Chl_c3, chlorophyll c3; chl_lide, chlorophyllide;
623 Fuco, fucoxanthin; Hex_19, 19'-hexanoyloxyfucoxanthin; Diadino, diadinoxanthin; Diato,
624 diatoxanthin.

625

626 In bottle incubation experiments conducted at station 27, the addition of Zn alone resulted
627 in the positive growth response of Chl b-containing algae (small green algae such as

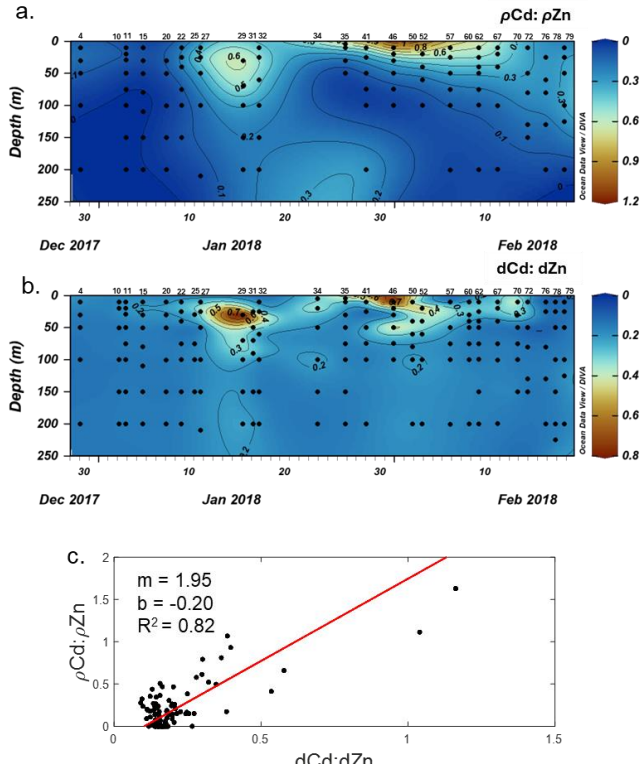


628 prasinophytes; (Kell et al. 2023), corroborating this finding. ρ Cd also positively correlated with
629 these Chl pigments but with slightly lower correlation Pearson correlation coefficients (cc = 0.3-
630 0.51; $p \leq .043$). Fucoxanthin (fuco) concentrations were more highly correlated with ρ Cd (cc =
631 0.57, $p = 4.3\text{e-}5$) than with ρ Zn (cc = 0.32, $p = 2.9\text{e-}2$), while the opposite was observed for 19'-
632 Hex (19'-hexanoyloxyfucoxanthin; cc = 0.54, $p = 1.1\text{e-}4$ for Zn; not significant for Cd) (**Fig.**
633 **11e**). Fuco and 19'-Hex are used as taxonomic indicators of diatoms and *Phaeocystis*,
634 respectively, in the Ross Sea (DiTullio and Smith 1995; DiTullio et al. 2003, 2007; Wright et al.
635 2010). The higher correlation coefficient between ρ Zn and *Phaeocystis* abundance (as indicated
636 by 19'-Hex) implies that Zn uptake was driven largely by *Phaeocystis*. This finding is consistent
637 with the detection of *Phaeocystis* ZCRP-A, a protein characterized as an algal Zn^{2+}
638 metallochaperone (Kellogg et al. 2022), in metaproteomic data collected from both the
639 incubation experiment and throughout the water column at station 27 (Kell et al. 2023). The
640 positive correlation between ρ Cd and the abundance of diatoms (as indicated by fuco) is
641 consistent with the diatomic utilization of Cd as a nutrient within CDCA metalloenzymes, as
642 *cdca* genes have, to date, been found exclusively in diatom species (Park et al., 2007, 2008).
643 While it is likely that both *Phaeocystis* and diatoms contributed to the Cd and Zn uptake rates
644 measured here, it is currently unknown if *Phaeocystis* can utilize Cd as a nutrient. Overall, any
645 potential growth benefit conferred by our Cd spike additions may only have been applicable to
646 diatoms that 1) possessed the *cdca* gene and 2) faced selection pressure to utilize Cd as a
647 cofactor in CDCA due to low seawater pCO_2 (as documented on this expedition) creating
648 enhanced demand for dZn. The presence of Cd-utilizing diatoms in the water column at station
649 27 was demonstrated by the detection of CDCA transcripts with closest taxonomic matches to
650 the diatom genera *Chaetoceros* and *Corethron* (Kell et al. 2023). Station 27 also exhibited high



651 surface Chl fluorescence (19.3 mg m⁻³ at 10 m), low pCO₂ (221 μ atm at 5 m), and high
652 maximum Zn and Cd uptake rates (46 and 20 pmol L⁻¹ d⁻¹, respectively), demonstrating a high
653 algal demand for Zn that likely created pressure for Cd uptake.

654 We next consider the effect of the depleted seawater pCO₂ levels induced by the high
655 biomass conditions observed on this expedition. Previously, a strong correlation between
656 dissolved $\delta^{114}\text{Cd}$ and dissolved CO₂ was documented in the Atlantic Sector of the Southern
657 Ocean (de Baar et al. 2017), suggesting significant Cd isotope fractionation due to biological
658 uptake into the particulate phase. A relationship between total surface Cd uptake rates at 10 m
659 and surface pCO₂ (underway, measured at 5 m) was not observed in the present study (**Fig. 11b**).
660 The present study includes measurements of total Cd uptake (that is, the sum of all Cd isotopes)
661 using an added Cd isotope tracer, and hence did not explore natural isotope fractionation effects.
662 However, we did observe a significant negative linear relationship between total Zn uptake rates
663 and seawater pCO₂ ($m = -0.58$; $R^2 = 0.63$; **Fig. 11a**) consistent with an increased demand for Zn²⁺
664 to power the carbon concentrating mechanism of photosynthetic algae under lower CO₂
665 availability. ρZn and ρCd furthermore shared a significant positive linear relationship with each
666 other ($m = 0.13$; $R^2 = 0.64$; **Fig. 11c**) (as was also reflected in the Pearson correlation test; PCC =
667 0.69, $p = 1.7\text{e-}7$, **Fig. 11d**) implying that as demand for Zn increased, demand for Cd also
668 increased, consistent with laboratory studies showing their co-transport in marine algae (Sunda
669 and Huntsman 2000). We also note that $\rho\text{Cd}:\rho\text{Zn}$ uptake ratios were higher (> 0.4) at the surface
670 where total dissolved dCd:dZn ratios were comparatively higher (> 0.3) (**Fig. 12a,b**). The strong
671 positive linear relationship shared between these ratios ($R^2 = 0.82$; **Fig. 12c**) further suggests that
672 dZn levels were depleted enough to induce increased Cd uptake rates, and is consistent with their
673 known biochemical substitution within marine algae.



674

675  **Figure 12.** (a) Cd:Zn uptake ratios ($\rho\text{Cd:}\rho\text{Zn}$) and (b) total dissolved Cd:Zn ratios ($\text{dCd:}\text{dZn}$) for
676 all stations during the CICLOPS expedition measured in the upper 250 m represented in color
677 scale and over time of sampling. (c) Two-way linear regression showing the positive relationship
678 between $\text{dCd:}\text{dZn}$ and $\rho\text{Cd:}\rho\text{Zn}$ inclusive of all stations and depth ($n=111$, $R^2 = 0.82$).
679

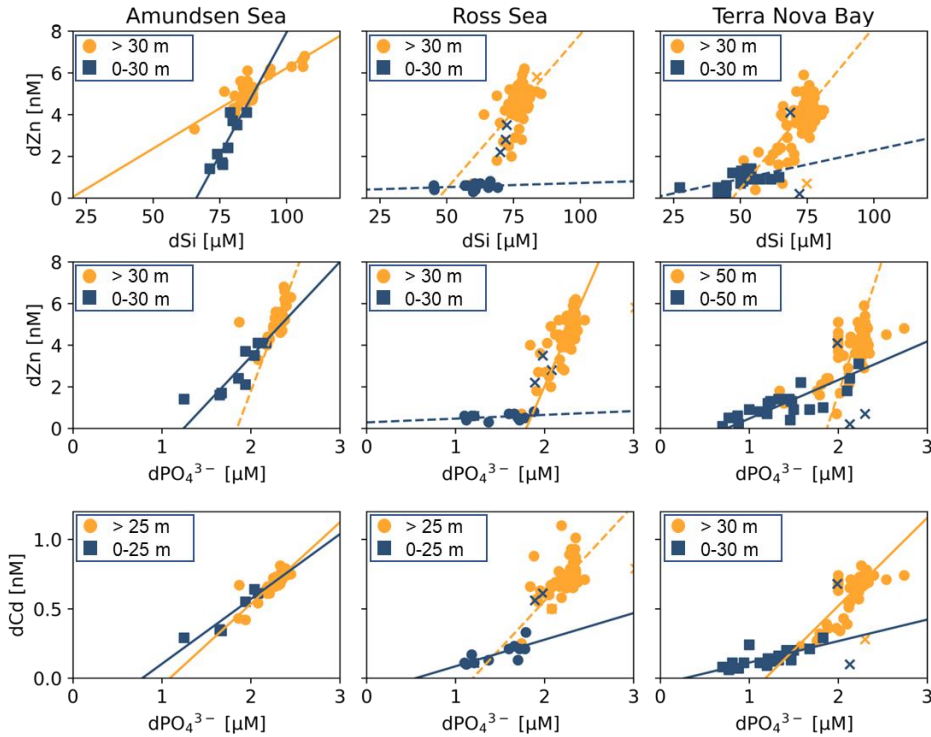
680 Algal Cd uptake rates are known to be inversely related to both Mn^{2+} and Zn^{2+}
681 concentrations in culture (Lee et al. 1995; Sunda and Huntsman 1996), which is thought to
682 reflect the uptake of Cd by two separate inducible transport systems. Cadmium is taken up
683 competitively by the high-affinity Zn uptake system under low Zn^{2+} conditions, as demonstrated
684 above, while Cd, Zn, and Mn share the same low-affinity Mn uptake system under high Zn^{2+}
685 conditions (Lee et al. 1995; Sunda and Huntsman 1998a; b, 2000; Xu et al. 2007). With the
686 exception of the Amundsen Sea stations, dMn was consistently observed at concentrations of
687 only 0.1-0.5 nM within the upper 50 m (**Fig. 3h**; **Fig. 5h**; **Fig. 7h**). Low surface dMn



688 concentrations within the Southern Ocean have been documented previously and were attributed
689 to a combination of biological uptake at the surface causing depletion and low resupply due to
690 few external sources (Latour et al. 2021). While ρ_{Cd} was negatively correlated with dMn (PCC
691 = -0.34, $p = 0.02$) considering all stations and all depths, ρ_{Cd} was more strongly negatively
692 correlated with dZn (PCC = -0.76, $p = 1.1\text{e-9}$), which was the strongest negative correlation
693 comparing all measured parameters to ρ_{Cd} (**Fig. 11d**). This finding is consistent with decreased
694 dCd uptake where dZn availability is sufficient. Overall, these results are consistent with biology
695 (total biomass) and pCO₂ acting as primary influences on ρ_{Zn} , with increases in ρ_{Zn} leading to
696 increases in ρ_{Cd} through the upregulation of a shared transport system.

697 **4.4 dZn and dCd relationships with macronutrients**

698 The growth of phytoplankton and bacteria in the shallow euphotic zone results in the
699 removal of bioactive trace metals and macronutrients from the dissolved phase into the
700 particulate phase, resulting in dissolved metal:macronutrient relationships that reflect their
701 collective stoichiometry (Horner et al. 2021). Positive linear slopes result generally indicate the
702 co-cycling of the metal and the macronutrient via uptake and remineralization, though slope
703 values can vary widely by basin as they are a function of the metal:macronutrient uptake and
704 remineralization stoichiometry of the native community and overall nutrient availability. Two-
705 way linear regressions (see Methods) were used to investigate the relationships between dZn and
706 dissolved silicate (dSi), dZn and dissolved phosphate (dP), and dCd and dP for the Amundsen
707 Sea, Ross Sea, and TNB station groups (**Fig. 13**).



708

709 **Figure 13.** Relationships between (Top row) total dissolved Zn and silicate (dSi), (Middle row)
710 total dissolved Zn and phosphate (dPO_4^{3-}), and (Bottom row) total dissolved Cd and dPO_4^{3-} for
711 surface (blue squares) and deep ocean (orange circles) arranged by station group (Amundsen
712 Sea, Ross Sea, and Terra Nova Bay). Depth thresholds were manually chosen to optimize the
713 linear fit of the surface and deep ocean trends. Regressions with an $R^2 \geq 0.50$ are shown as a
714 solid line, and those with an $R^2 < 0.50$ are shown as a dotted line. See **Table S4** for
715 stoichiometric parameters and values. Regression outliers are marked with an 'x'. Data originally
716 plotted in Chmiel et al. 2023 and reprised here for ease of comparison with dZn:Si data.
717

718

The dZn:dP and dCd:dP relationships from this expedition were originally presented in

719

Chmiel et al. 2023 for comparison to dCo:dP, while they are included in the present study for

720

ease of comparison with dZn:dSi relationships presented for the first time. For these analyses, the

721

depth threshold that separates the surface and deep ocean was manually defined in order to

722

optimize the linear fit of the surface versus deep trends— this threshold depth can be thought of



723 as an inflection point that represents the largest change in trace metal concentration with respect
724 to dP or dSi concentration (Chmiel et al. 2023).

725 As noted above, the near-linear global dZn:dSi relationship (Bruland et al. 1978; Vance
726 et al. 2017; Middag et al. 2019) has been posited to arise, in part, from faster drawdown of Zn
727 and Si relative to dPO₄³⁻ into Southern Ocean diatoms that leaves surface waters Zn and Si

728 depleted (Vance et al. 2017). We observed distinct differences in dissolved dZn:dSi ecological
729 stoichiometries comparing Amundsen Sea, Ross Sea and Terra Nova Bay station groups (**Fig.**

730 **13; Table S4**). A positive linear dZn:dSi relationship with a steep ($m = 0.23 \pm 0.05$; **Table S4**)

731 slope observed in the upper ocean of the Amundsen Sea contrasted starkly with the shallow

732 slopes observed in the upper ocean of the Ross Sea and Terra Nova Bay. A bloom of non-

733 silicifying *Phaeocystis antarctica* was present during our passage through the Amundsen Sea,

734 consistent with abundant silicic acid yet rapid drawn down of Zn, which is known to be used by

735 this organism (Saito and Goepfert 2008). In contrast, the shallow slopes in the Ross Sea and

736 Terra Nova Bay resulted from the persistence of dSi concentrations $\geq 30 \mu\text{M}$ in the upper 30 m

737 while dZn was reduced to sub-nanomolar concentrations (average dZn = $0.87 \pm 0.42 \text{ nM}$ in TNB

738 at 10 m depth, n= 11), highlighting the intense drawdown of dZn by biota in this region to meet a

739 high metabolic dZn demand.

740 Similar trends were observed for dZn:dP and dCd:P, which exhibited shallow slopes

741 within the upper ocean of the Ross Sea and Terra Nova Bay. Southern Ocean diatoms are known

742 to have Zn:P uptake ratios that are up to an order of magnitude greater than the average for

743 oceanic phytoplankton (Twining and Baines 2013; Vance et al. 2017; Sieber et al. 2020). The

744 increased presence of diatoms (as indicated by higher fucoxanthin concentrations) at the late

745 stations within Terra Nova Bay therefore likely exacerbated the surface decoupling of dZn and



746 dP due to their high dZn demand. The maximum uptake rates of 158, 115, and 89 pmol Zn L⁻¹ d⁻¹
747 measured in this study for the Amundsen Sea, Ross Sea, and Terra Nova Bay groups,
748 respectively, contextualize the high Zn uptake rates hypothesized to contribute to the high dZn:
749 dP uptake ratios observed in Southern Ocean diatoms. These rates are indicative of total potential
750 biological uptake, likely influenced by a depleted labile Zn pool and residual of complexed Zn,
751 that then results in low dZn:dP ratios in shallow waters.

752 Like dZn and dSi, dCd and dP concentrations are known to share strong correlations in
753 both deep and surface seawater (Boyle et al. 1976; Boyle 1988; de Baar et al. 1994), with the
754 vertical distribution of Cd controlled by phytoplankton uptake in surface waters and sinking of
755 particulate organic matter and subsequent remineralization at depth. Observations of enhanced
756 Cd uptake within the Fe-limited Southern Ocean (Cullen 2006) are consistent with observations
757 of increased Cd uptake by marine algal species under Fe limitation in both the field (Cullen et al.
758 2003; Cullen and Sherrell 2005; Baars et al. 2014) and in culture (Sunda and Huntsman 2000;
759 Lane et al. 2009), thought to be due to the increased use of Cd in biochemical processes or
760 inadvertent uptake due to the upregulation of metal transporters (Sunda and Huntsman 2000;
761 Cullen 2006). In these coastal regions, dCd:dP had the same regional and depth trends as dZn:dP,
762 further demonstrating their close biogeochemical association.

763 **5 Conclusions**

764 We have quantified the movement of the trace metals Zn and Cd from the dissolved to
765 the particulate phase within the phytoplankton >3 µm size fraction collected in the Amundsen
766 Sea, Ross Sea, and Terra Nova Bay of the Southern Ocean during austral summer 2017-2018.
767 Increases in particulate ¹¹⁰Cd and ⁶⁷Zn concentrations in spiked samples, increases in particulate
768 ⁶⁷Zn:⁶⁸Zn and ¹¹⁰Cd:¹¹⁴Cd sample ratios relative to controls, and surface depletion of total



769 dissolved Zn and Cd concentrations apparent at all 18 stations demonstrated metal uptake into
770 the particulate phase mainly within the upper 50 m. Our study confirms the utility of the 24hr Cd
771 stable isotope tracer uptake method employed previously (Cox et al. 2014) and expands its use to
772 measurements of Zn uptake. Notably, maximum Cd uptake rates measured in the present study
773 were 3.4, 3.7, and 3.3 times higher in the Amundsen Sea, Ross Sea, and Terra Nova Bay,
774 respectively, compared to the maximum Cd uptake rate of $6.1 \text{ pmol L}^{-1} \text{ d}^{-1}$ measured previously
775 within the Costa Rica Dome using identical methods (Cox et al. 2014), demonstrating the
776 influence of high productivity and the native community on the flux of dCd into the particulate
777 phase.

778 The highly productive phytoplankton bloom documented in the study area resulted in an
779 intense algal Zn demand within the surface ocean, which we have quantified via uptake rate
780 measurements. This intense Zn demand shifted the demand for other trace metal micronutrients
781 as well, namely Cd and cobalt (Co) (Chmiel et al. 2023). Due to their similar charge and atomic
782 radii, Zn^{2+} , Co^{2+} and Cd^{2+} cations often share the same transporter uptake systems. An
783 organism's ability to utilize these metals as metabolic cofactors is influenced by their
784 environment and the affinity of the uptake ligands for each metal cation (Irving and Williams
785 1953; Sunda and Huntsman 1992). When dZn availability is low, more dCd and dCo are able to
786 bind transport ligands. Therefore, dZn concentrations and cycling can influence the cycling of
787 dCd and dCo, particularly in low dZn environments as documented for dCd in the present study.
788 The influence of dZn cycling on dCo distributions in this region was also documented for the
789 same expedition, with evidence for high rates of biological Co uptake in the Ross Sea driven by
790 dZn (and vitamin B₁₂) scarcity (Chmiel et al. 2023). The high Zn uptake rates measured in this
791 study therefore not only demonstrate a mechanism for the depletion of abundant Zn in coastal



792 areas with the potential for Zn scarcity during highly productive bloom events, but also reveal
793 dynamic changes in the cycling of Cd and Co as a consequence of high Zn demand.

794

795 *Data availability*

796 CICLOPS (NBP18-01) CTD hydrography data (including pressure, temperature, total
797 dissolved oxygen, conductivity, fluorescence, and beam transmission; [https://www.bco-
798 dmo.org/dataset-deployment/783917](https://www.bco-dmo.org/dataset-deployment/783917)) in addition to total dissolved metal, Zn and Cd uptake rate,
799 macronutrient, and pigment datasets are available through the NSF Biological and Chemical
800 Oceanography Data Management Office (BCO-DMO) repository ([https://www.bco-
801 dmo.org/deployment/778919](https://www.bco-dmo.org/deployment/778919)). Underway pCO₂ data collected during cruise NBP1801 is
802 available through R2R, <https://doi.org/10.7284/139318>.

803 *Author contributions*

804 Conceptualization and analysis of the study was carried out by RMK and MAS. This work
805 was supervised by MAS and GRD. Funding was acquired by MAS and GRD. All co-authors
806 contributed to data collection. RMK and MAS wrote the manuscript with review and editing
807 contributions from all co-authors.

808 *Competing interests*

809 The authors declare that they have no conflict of interest.

810 *Acknowledgements*

811 We thank the captain, crew, marine technicians, and science party of RVIB Nathaniel B.
812 Palmer for their support and contributions to the success of the NBP18-01 cruise, Joe Jennings
813 (OSU) for conducting macronutrient analyses, Lauren Lees for assistance with sampling, and
814 Natalie Cohen for assistance in operation of the seaFAST and application of the isotope dilution
815 technique.



816 *Funding*

817 National Science Foundation grant 2123055 (MAS)

818 National Science Foundation grant 2125063 (MAS)

819 National Science Foundation grant 1643684 (MAS)

820 National Science Foundation grant 1924554 (MAS)

821 National Science Foundation grant NSF-PLR 1643845 (RBD)

822 Simons Foundation (MAS)

823 National Science Foundation grant NSF-OPP 1644073 (GRD)

824 TJH acknowledges support from the Woods Hole Oceanographic Institution's *Ocean and*

825 *Climate Innovation Accelerator* program.

826 **References**

827 Arrigo, K. R., G. L. van Dijken, and S. Bushinsky. 2008. Primary production in the Southern
828 Ocean, 1997–2006. *Journal of Geophysical Research* **113**: C08004.

829 doi:10.1029/2007JC004551

830 Arrigo, K. R., K. E. Lowry, and G. L. van Dijken. 2012. Annual changes in sea ice and
831 phytoplankton in polynyas of the Amundsen Sea, Antarctica. *Deep Sea Research Part II:*
832 *Topical Studies in Oceanography* **71–76**: 5–15. doi:10.1016/j.dsr2.2012.03.006

833 de Baar, H. J. W., S. M. A. C. van Heuven, W. Abouchami, Z. Xue, S. J. G. Galer, M.

834 Rehkämper, R. Middag, and J. van Ooijen. 2017. Interactions of dissolved CO₂ with
835 cadmium isotopes in the Southern Ocean. *Marine Chemistry* **195**: 105–121.

836 doi:10.1016/J.MARCHEM.2017.06.010

837 de Baar, H. J. W., P. M. Saager, R. F. Nolting, and J. van der Meer. 1994. Cadmium versus
838 phosphate in the world ocean. *Marine Chemistry*. doi:10.1016/0304-4203(94)90082-5



839 Baars, O., W. Abouchami, S. J. G. Galer, M. Boye, and P. L. Croot. 2014. Dissolved cadmium in
840 the Southern Ocean: Distribution, speciation, and relation to phosphate. Limnology and
841 Oceanography **59**: 385–399. doi:10.4319/LO.2014.59.2.0385

842 Bertrand, E. M., M. A. Saito, J. M. Rose, C. R. Riesselman, M. C. Lohan, A. E. Noble, P. A.
843 Lee, and G. R. DiTullio. 2007. Vitamin B 12 and iron colimitation of phytoplankton
844 growth in the Ross Sea. Limnology and Oceanography **52**: 1079–1093.
845 doi:10.4319/lo.2007.52.3.1079

846 Biller, D. V., and K. W. Bruland. 2012. Analysis of Mn, Fe, Co, Ni, Cu, Zn, Cd, and Pb in
847 seawater using the Nobias-chelate PA1 resin and magnetic sector inductively coupled
848 plasma mass spectrometry (ICP-MS). Marine Chemistry.
849 doi:10.1016/j.marchem.2011.12.001

850 Bishop, J. K. B., and T. J. Wood. 2009. Year-round observations of carbon biomass and flux
851 variability in the Southern Ocean. Global Biogeochemical Cycles.
852 doi:10.1029/2008GB003206

853 Bown, J., P. Laan, S. Ossebaar, K. Bakker, P. Rozema, and H. J. W. de Baar. 2017. Bioactive
854 trace metal time series during Austral summer in Ryder Bay, Western Antarctic
855 Peninsula. Deep-Sea Research Part II: Topical Studies in Oceanography.
856 doi:10.1016/j.dsr2.2016.07.004

857 Boyle, E. A. 1988. Cadmium: Chemical tracer of deepwater paleoceanography.
858 Paleoceanography. doi:10.1029/PA003i004p00471

859 Boyle, E. A., F. Sclater, and J. M. Edmond. 1976. On the marine geochemistry of cadmium.
860 Nature. doi:10.1038/263042a0



861 Brand, L. E., W. G. Sunda, and R. R. L. Guillard. 1986. Reduction of marine phytoplankton
862 reproduction rates by copper and cadmium. *Journal of Experimental Marine Biology and*
863 *Ecology*. doi:10.1016/0022-0981(86)90205-4

864 Bruland, K. W., G. A. Knauer, and J. H. Martin. 1978. Zinc in north-east Pacific water. *Nature*
865 **271**: 741–743. doi:10.1038/271741a0

866 Chmiel, R. J., R. M. Kell, D. Rao, D. M. Moran, G. R. DiTullio, and M. A. Saito. 2023. Low
867 cobalt inventories in the Amundsen and Ross seas driven by high demand for labile
868 cobalt uptake among native phytoplankton communities. *Biogeosciences* **20**: 3997–4027.
869 doi:10.5194/bg-20-3997-2023

870 Cox, A. D., A. E. Noble, and M. A. Saito. 2014. Cadmium enriched stable isotope uptake and
871 addition experiments with natural phytoplankton assemblages in the Costa Rica
872 Upwelling Dome. *Marine Chemistry*. doi:10.1016/j.marchem.2014.09.009

873 Cramer, F. 2023. Scientific colour maps. doi:10.5281/ZENODO.1243862

874 Cullen, J. T. 2006. On the nonlinear relationship between dissolved cadmium and phosphate in
875 the modern global ocean: Could chronic iron limitation of phytoplankton growth cause
876 the kink? *Limnology and Oceanography* **51**: 1369–1380. doi:10.4319/lo.2006.51.3.1369

877 Cullen, J. T., Z. Chase, K. H. Coale, S. E. Fitzwater, and R. M. Sherrell. 2003. Effect of iron
878 limitation on the cadmium to phosphorus ratio of natural phytoplankton assemblages
879 from the Southern Ocean. *Limnology and Oceanography*. doi:10.4319/lo.2003.48.3.1079

880 Cullen, J. T., T. W. Lane, F. M. M. Morel, and R. M. Sherrell. 1999. Modulation of cadmium
881 uptake in phytoplankton by seawater CO₂ concentration. *Nature*. doi:10.1038/46007



882 Cullen, J. T., and R. M. Sherrell. 2005. Effects of dissolved carbon dioxide, zinc, and manganese
883 on the cadmium to phosphorus ratio in natural phytoplankton assemblages. *Limnology*
884 and *Oceanography* **50**: 1193–1204. doi:10.4319/lo.2005.50.4.1193

885 Cutter, G. A., and K. W. Bruland. 2012. Rapid and noncontaminating sampling system for trace
886 elements in global ocean surveys. *Limnology and Oceanography: Methods*.
887 doi:10.4319/lom.2012.10.425

888 Das, P., S. Samantaray, and G. R. Rout. 1997. Studies on cadmium toxicity in plants: A review.
889 *Environmental Pollution*. doi:10.1016/S0269-7491(97)00110-3

890 DiTullio, G. R., N. Garcia, S. F. Riseman, and P. N. Sedwick. 2007. Effects of iron concentration
891 on pigment composition in *Phaeocystis antarctica* grown at low irradiance.
892 *Biogeochemistry* **83**: 71–81. doi:10.1007/s10533-007-9080-8

893 DiTullio, G. R., M. E. Geesey, A. Leventer, and M. P. Lizotte. 2003. Algal pigment ratios in the
894 Ross Sea: Implications for Chemtax analysis of Southern Ocean data, p. 35–51. *In*.
895 DiTullio, G. R., and W. O. Smith. 1995. Relationship between dimethylsulfide and
896 phytoplankton pigment concentrations in the Ross Sea, Antarctica. *Deep-Sea Research*
897 Part I. doi:10.1016/0967-0637(95)00051-7

898 Ellwood, M. J. 2008. Wintertime trace metal (Zn, Cu, Ni, Cd, Pb and Co) and nutrient
899 distributions in the Subantarctic Zone between 40–52°S; 155–160°E. *Marine Chemistry*.
900 doi:10.1016/j.marchem.2008.07.008

901 Ellwood, M. J., and K. A. Hunter. 2000. The incorporation of zinc and iron into the frustule of
902 the marine diatom *Thalassiosira pseudonana*. *Limnology and Oceanography*.
903 doi:10.4319/lo.2000.45.7.1517



904 Fitzwater, S. E., K. S. Johnson, R. M. Gordon, K. H. Coale, and W. O. Smith. 2000. Trace metal
905 concentrations in the Ross Sea and their relationship with nutrients and phytoplankton
906 growth. *Deep-Sea Research Part II: Topical Studies in Oceanography* **47**: 3159–3179.
907 doi:10.1016/S0967-0645(00)00063-1

908 Gerringa, L. J. A., A.-C. Alderkamp, G. van Dijken, P. Laan, R. Middag, and K. R. Arrigo. 2020.
909 Dissolved Trace Metals in the Ross Sea. *Frontiers in Marine Science* **7**.
910 doi:10.3389/fmars.2020.577098

911 Giordano, R., G. Lombardi, L. Ciaralli, E. Beccaloni, A. Sepe, M. Ciprotti, and S. Costantini.
912 1999. Major and trace elements in sediments from Terra Nova Bay, Antarctica. *Science*
913 of The Total Environment **227**: 29–40. doi:10.1016/S0048-9697(98)00402-1

914 Haas, C. E., D. A. Rodionov, J. Kropat, D. Malasarn, S. S. Merchant, and V. de Crécy-Lagard.
915 2009. A subset of the diverse COG0523 family of putative metal chaperones is linked to
916 zinc homeostasis in all kingdoms of life. *BMC Genomics* **10**: 470. doi:10.1186/1471-
917 2164-10-470

918 Hopwood, M. J., D. Carroll, J. Höfer, and others. 2019. Highly variable iron content modulates
919 iceberg-ocean fertilisation and potential carbon export. *Nature Communications* 2019
920 10:1 **10**: 1–10. doi:10.1038/s41467-019-13231-0

921 Horner, T. J., R. B. Y. Lee, G. M. Henderson, and R. E. M. Rickaby. 2013. Nonspecific uptake
922 and homeostasis drive the oceanic cadmium cycle. *Proceedings of the National Academy*
923 *of Sciences* **110**: 2500–2505. doi:10.1073/pnas.1213857110

924 Horner, T. J., S. H. Little, T. M. Conway, and others. 2021. Bioactive Trace Metals and Their
925 Isotopes as Paleoproductivity Proxies: An Assessment Using GEOTRACES-Era Data.
926 *Global Biogeochemical Cycles* **35**: e2020GB006814. doi:10.1029/2020GB006814



927 Hutchins, D. A., and K. W. Bruland. 1995. Fe, Zn, Mn and N transfer between size classes in a
928 coastal phytoplankton community: Trace metal and major nutrient recycling compared.
929 issn: 0022-2402 **53**: 297–313. doi:10.1357/0022240953213197

930 Hutchins, D. A., W. X. Wang, M. A. Schmidt, and N. S. Fisher. 1999. Dual-labeling techniques
931 for trace metal biogeochemical investigations in aquatic plankton communities. *Aquatic
932 Microbial Ecology*. doi:10.3354/ame019129

933 Hutchins, D., and K. Bruland. 1994. Grazer-mediated regeneration and assimilation of Fe, Zn
934 and Mn from planktonic prey. *Mar. Ecol. Prog. Ser.* **110**: 259–269.
935 doi:10.3354/meps110259

936 Irving, B. H., and R. J. P. Williams. 1953. The Stability of Transition-metal Complexes. *Journal
937 of the Chemical Society (Resumed)*. doi:10.1039/JR9530003192

938 Jackson, S. L., J. Spence, D. J. Janssen, A. R. S. Ross, and J. T. Cullen. 2018. Determination of
939 Mn, Fe, Ni, Cu, Zn, Cd and Pb in seawater using offline extraction and triple quadrupole
940 ICP-MS/MS. *Journal of Analytical Atomic Spectrometry* **33**: 304–313.
941 doi:10.1039/c7ja00237h

942 Kell, R. M., A. V. Subhas, N. L. Schanke, and others. 2023. Zinc stimulation of phytoplankton in
943 a low carbon dioxide, coastal Antarctic environment. doi:10.1101/2023.11.05.565706

944 Kellogg, R. M., M. A. Moosburner, N. R. Cohen, and others. 2022. Adaptive responses of
945 marine diatoms to zinc scarcity and ecological implications. *Nature Communications*
946 2022 **13**: 1–13. doi:10.1038/s41467-022-29603-y

947 Lane, E. S., D. M. Semeniuk, R. F. Strzepek, J. T. Cullen, and M. T. Maldonado. 2009. Effects
948 of iron limitation on intracellular cadmium of cultured phytoplankton: Implications for



949 surface dissolved cadmium to phosphate ratios. *Marine Chemistry* **115**: 155–162.

950 doi:10.1016/J.MARCHEM.2009.07.008

951 Lane, T. W., M. A. Saito, G. N. George, I. J. Pickering, R. C. Prince, and F. M. M. Morel. 2005.

952 A cadmium enzyme from a marine diatom. *Nature* **435**: 42–42. doi:10.1038/435042a

953 Latour, P., K. Wuttig, P. van der Merwe, and others. 2021. Manganese biogeochemistry in the

954 Southern Ocean, from Tasmania to Antarctica. *Limnology and Oceanography* **66**: 2547–

955 2562. doi:10.1002/lo.11772

956 Lee, J. G., S. B. Roberts, and F. M. M. Morel. 1995. Cadmium: A nutrient for the marine diatom

957 *Thalassiosira weissflogii*. *Limnology and Oceanography*. doi:10.4319/lo.1995.40.6.1056

958 Lee, J., and F. Morel. 1995. Replacement of zinc by cadmium in marine phytoplankton. *Marine*

959 *Ecology Progress Series* **127**: 305–309. doi:10.3354/meps127305

960 Lohan, M. C., P. J. Statham, and D. W. Crawford. 2002. Total dissolved zinc in the upper water

961 column of the subarctic North East Pacific. *Deep Sea Research Part II: Topical Studies in*

962 *Oceanography* **49**: 5793–5808. doi:10.1016/S0967-0645(02)00215-1

963 Martin, J. H. 1990. Glacial-interglacial CO₂ change: The Iron Hypothesis. *Paleoceanography*.

964 doi:10.1029/PA005i001p00001

965 Middag, R., H. J. W. Baar, and K. W. Bruland. 2019. The relationships between dissolved zinc

966 and major nutrients phosphate and silicate along the GEOTRACES GA02 transect in the

967 West Atlantic Ocean. *Global Biogeochemical Cycles* **33**: 63–84.

968 doi:10.1029/2018GB006034

969 Morel, F. M. M., P. J. Lam, and M. A. Saito. 2020. Trace metal substitution in marine

970 phytoplankton. *Annual Review of Earth and Planetary Sciences* **48**: 491–517.

971 doi:10.1146/annurev-earth-053018-060108



972 Morel, F. M. M., A. J. Milligan, and M. A. Saito. 2013. Marine Bioinorganic Chemistry: The
973 Role of Trace Metals in the Oceanic Cycles of Major Nutrients, *In* Treatise on
974 Geochemistry: Second Edition.

975 Morel, F. M. M., J. R. Reinfelder, S. B. Roberts, C. P. Chamberlain, J. G. Lee, and D. Yee. 1994.
976 Zinc and carbon co-limitation of marine phytoplankton. *Nature* **369**: 740–742.
977 doi:10.1038/369740A0

978 Noble, A. E., C. H. Lamborg, D. C. Ohnemus, and others. 2012. Basin-scale inputs of cobalt,
979 iron, and manganese from the Benguela-Angola front to the South Atlantic Ocean.
980 Limnology and Oceanography. doi:10.4319/lo.2012.57.4.0989

981 Noble, A. E., D. M. Moran, A. E. Allen, and M. A. Saito. 2013. Dissolved and particulate trace
982 metal micronutrients under the McMurdo Sound seasonal sea ice: basal sea ice
983 communities as a capacitor for iron. *Frontiers in Chemistry* **1**.
984 doi:10.3389/fchem.2013.00025

985 Ohnemus, D. C., S. Rauschenberg, G. A. Cutter, J. N. Fitzsimmons, R. M. Sherrell, and B. S.
986 Twining. 2017. Elevated trace metal content of prokaryotic communities associated with
987 marine oxygen deficient zones. *Limnology and Oceanography*. doi:10.1002/lo.10363

988 Oldham, V. E., R. Chmiel, C. M. Hansel, G. R. DiTullio, D. Rao, and M. Saito. 2021. Inhibited
989 Manganese Oxide Formation Hinders Cobalt Scavenging in the Ross Sea. *Global
990 Biogeochemical Cycles* **35**. doi:10.1029/2020GB006706

991 Park, H., P. J. McGinn, and F. M. M. Morel. 2008. Expression of cadmium carbonic anhydrase
992 of diatoms in seawater. *Aquatic Microbial Ecology*. doi:10.3354/ame01192



993 Park, H., B. Song, and F. M. M. Morel. 2007. Diversity of the cadmium-containing carbonic
994 anhydrase in marine diatoms and natural waters. *Environmental Microbiology*.
995 doi:10.1111/j.1462-2920.2006.01151.x

996 Person, R., M. Vancoppenolle, O. Aumont, and M. Malsang. 2021. Continental and Sea Ice Iron
997 Sources Fertilize the Southern Ocean in Synergy. *Geophysical Research Letters* **48**:
998 e2021GL094761. doi:10.1029/2021GL094761

999 Price, N. M., and F. M. M. Morel. 1990. Cadmium and cobalt substitution for zinc in a marine
1000 diatom. *Nature* **344**: 658–660. doi:10.1038/344658a0

1001 Rapp, I., C. Schlosser, D. Rusiecka, M. Gledhill, and E. P. Achterberg. 2017. Automated
1002 preconcentration of Fe, Zn, Cu, Ni, Cd, Pb, Co, and Mn in seawater with analysis using
1003 high-resolution sector field inductively-coupled plasma mass spectrometry. *Analytica
1004 Chimica Acta*. doi:10.1016/j.aca.2017.05.008

1005 Roshan, S., T. DeVries, J. Wu, and G. Chen. 2018. The Internal Cycling of Zinc in the Ocean.
1006 *Global Biogeochemical Cycles* **32**: 1833–1849. doi:10.1029/2018GB006045

1007 Rudge, J. F., B. C. Reynolds, and B. Bourdon. 2009. The double spike toolbox. *Chemical
1008 Geology*. doi:10.1016/j.chemgeo.2009.05.010

1009 Saito, M. A., and T. J. Goepfert. 2008. Zinc-cobalt colimitation of *Phaeocystis antarctica*.
1010 *Limnology and Oceanography* **53**: 266–275. doi:10.4319/lo.2008.53.1.0266

1011 Sedwick, P. N., G. R. Di Tullio, and D. J. Mackey. 2000. Iron and manganese in the Ross Sea,
1012 Seasonal iron limitation in Antarctic. *Journal of Geophysical Research: Oceans*.
1013 doi:10.1029/2000JC000256

1014 Sedwick, P. N., C. M. Marsay, B. M. Sohst, and others. 2011. Early season depletion of
1015 dissolved iron in the Ross Sea polynya: Implications for iron dynamics on the Antarctic



1016 continental shelf. *Journal of Geophysical Research* **116**: C12019.

1017 doi:10.1029/2010JC006553

1018 Shaked, Y., Y. Xu, K. Leblanc, and F. M. M. Morel. 2006. Zinc availability and alkaline
1019 phosphatase activity in *Emiliania huxleyi*: Implications for Zn-P co-limitation in the
1020 ocean. *Limnology and Oceanography* **51**: 299–309. doi:10.4319/lo.2006.51.1.0299

1021 Sieber, M., T. M. Conway, G. F. de Souza, C. S. Hassler, M. J. Ellwood, and D. Vance. 2020.
1022 Cycling of zinc and its isotopes across multiple zones of the Southern Ocean: Insights
1023 from the Antarctic Circumnavigation Expedition. *Geochimica et Cosmochimica Acta*.
1024 doi:10.1016/j.gca.2019.09.039

1025 Sohrin, Y., S. Urushihara, S. Nakatsuka, T. Kono, E. Higo, T. Minami, K. Norisuye, and S.
1026 Umetani. 2008. Multielemental determination of GEOTRACES key trace metals in
1027 seawater by ICPMS after preconcentration using an ethylenediaminetriacetic acid
1028 chelating resin. *Analytical Chemistry*. doi:10.1021/ac800500f

1029 de Souza, G. F., S. P. Khatiwala, M. P. Hain, S. H. Little, and D. Vance. 2018. On the origin of
1030 the marine zinc–silicon correlation. *Earth and Planetary Science Letters* **492**: 22–34.
1031 doi:10.1016/j.epsl.2018.03.050

1032 St-Laurent, P., P. L. Yager, R. M. Sherrell, S. E. Stammerjohn, and M. S. Dinniman. 2017.
1033 Pathways and supply of dissolved iron in the Amundsen Sea (Antarctica). *Journal of
1034 Geophysical Research: Oceans* **122**: 7135–7162. doi:10.1002/2017JC013162

1035 Sunda, W. G., and S. A. Huntsman. 1992. Feedback interactions between zinc and phytoplankton
1036 in seawater. *Limnology and Oceanography* **37**: 25–40. doi:10.4319/lo.1992.37.1.0025



1037 Sunda, W. G., and S. A. Huntsman. 1995. Cobalt and zinc interreplacement in marine
1038 phytoplankton: Biological and geochemical implications. *Limnology and Oceanography*
1039 **40**: 1404–1417. doi:10.4319/lo.1995.40.8.1404

1040 Sunda, W. G., and S. A. Huntsman. 1996. Antagonisms between cadmium and zinc toxicity and
1041 manganese limitation in a coastal diatom. *Limnology and Oceanography* **41**: 373–387.
1042 doi:10.4319/lo.1996.41.3.0373

1043 Sunda, W. G., and S. A. Huntsman. 1998a. Processes regulating cellular metal accumulation and
1044 physiological effects: Phytoplankton as model systems. *Science of The Total
1045 Environment* **219**: 165–181. doi:10.1016/S0048-9697(98)00226-5

1046 Sunda, W. G., and S. A. Huntsman. 1998b. Control of Cd Concentrations in a Coastal Diatom by
1047 Interactions among Free Ionic Cd, Zn, and Mn in Seawater. *Environmental Science &
1048 Technology* **32**: 2961–2968. doi:10.1021/es980271y

1049 Sunda, W. G., and S. A. Huntsman. 2000. Effect of Zn, Mn, and Fe on Cd accumulation in
1050 phytoplankton: Implications for oceanic Cd cycling. *Limnology and Oceanography* **45**:
1051 1501–1516. doi:10.4319/lo.2000.45.7.1501

1052 Tan, D., W. Xu, Z. Zhu, S. Li, G. Wu, and H. Qin. 2020. Optimizing the ratio of the spike to
1053 sample for isotope dilution analysis: a case study with selenium isotopes. *Acta
1054 Geochimica*. doi:10.1007/s11631-019-00390-6

1055 Twining, B. S., and S. B. Baines. 2013. The trace metal composition of marine phytoplankton.
1056 *Annual review of marine science* **5**: 191–215. doi:10.1146/annurev-marine-121211-
1057 172322



1058 Twining, B. S., S. B. Baines, and N. S. Fisher. 2004. Element stoichiometries of individual
1059 plankton cells collected during the Southern Ocean Iron Experiment (SOFeX).
1060 *Limnology and Oceanography* **49**: 2115–2128. doi:10.4319/LO.2004.49.6.2115
1061 Twining, B. S., S. D. Nodder, A. L. King, and others. 2014. Differential remineralization of
1062 major and trace elements in sinking diatoms. *Limnology and Oceanography* **59**: 689–704.
1063 doi:10.4319/LO.2014.59.3.0689
1064 Vance, D., S. H. Little, G. F. De Souza, S. Khatiwala, M. C. Lohan, and R. Middag. 2017.
1065 Silicon and zinc biogeochemical cycles coupled through the Southern Ocean. *Nature
1066 Geoscience* **10**: 202–206. doi:10.1038/NGEO2890
1067 Weber, T., S. John, A. Tagliabue, and T. DeVries. 2018. Biological uptake and reversible
1068 scavenging of zinc in the global ocean. *Science* **361**: 72–76.
1069 doi:10.1126/SCIENCE.AAP8532
1070 Wright, S. W., R. L. van den Enden, I. Pearce, A. T. Davidson, F. J. Scott, and K. J. Westwood.
1071 2010. Phytoplankton community structure and stocks in the Southern Ocean (30–80°E)
1072 determined by CHEMTAX analysis of HPLC pigment signatures. *Deep-Sea Research
1073 Part II: Topical Studies in Oceanography*. doi:10.1016/j.dsr2.2009.06.015
1074 Wu, J., and E. A. Boyle. 1998. Determination of iron in seawater by high-resolution isotope
1075 dilution inductively coupled plasma mass spectrometry after Mg(OH)2 coprecipitation.
1076 *Analytica Chimica Acta* **367**: 183–191. doi:10.1016/S0003-2670(98)00145-7
1077 Wuttig, K., A. T. Townsend, P. van der Merwe, and others. 2019. Critical evaluation of a
1078 seaFAST system for the analysis of trace metals in marine samples. *Talanta*.
1079 doi:10.1016/j.talanta.2019.01.047



1080 Xu, Y., D. Tang, Y. Shaked, and F. M. M. Morel. 2007. Zinc, cadmium, and cobalt
1081 interreplacement and relative use efficiencies in the coccolithophore *Emiliania huxleyi*.
1082 *Limnology and Oceanography* **52**: 2294–2305. doi:10.4319/lo.2007.52.5.2294
1083 Zhao, Y., D. Vance, W. Abouchami, and H. J. W. de Baar. 2014. Biogeochemical cycling of zinc
1084 and its isotopes in the Southern Ocean. *Geochimica et Cosmochimica Acta*.
1085 doi:10.1016/j.gca.2013.07.045
1086